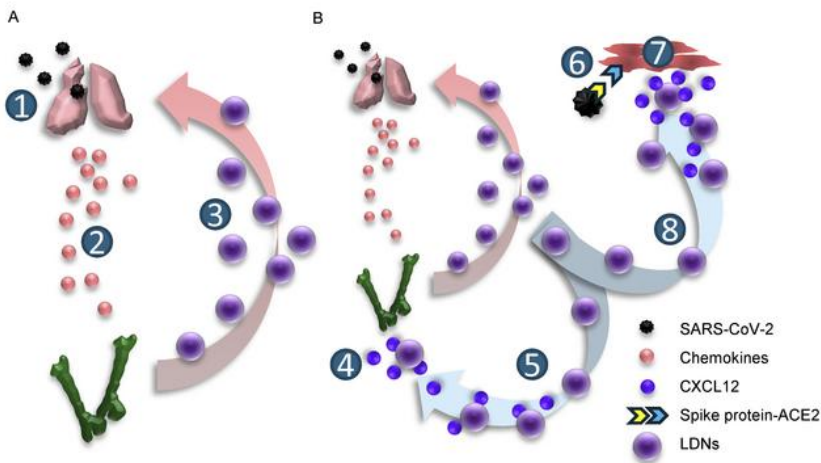# CXCL12 ameliorates neutrophilia and disease severity in SARS-CoV-2 infection

Jian Zheng, … , Jun Yan, Stanley Perlman

Research | In-Press Preview | COVID-19 | Infectious disease

Graphical abstract

Graphical Abstract
A. SARS-CoV-2 infection ① induces chemokines ②, which causes LDNs to migrate from bone marrow to lung ③.
B. Bone marrow-derived CXCL12 ④ reduces lung infiltration of LDNs by attracting LDNs ⑤. In addition, the interaction between SARS-CoV-2 spike protein and ACE2 ⑥ results in CXCL12 expression by endothelial cells ⑦, keeping LDNs in the vasculature ⑧.

Find the latest version:

https://jci.me/188222/pdf

CXCL12 ameliorates neutrophilia and disease severity in SARS-CoV-2 infection

Jian Zheng[1,2,3]*, Hima Dhakal[1], Enya Qing[4], Rejeena Shrestha[1,5], Anne E. Geller[1,5], Samantha M. Morrissey[1,5], Divyasha Saxena[2], Xiaoling Hu[5], Hong Li[6], Haiyan Li[5], Kevin Wilhelmsen[7], Linder H Wendt[8], Klaus Klumpp[7], Patrick S. Hume[9,10], William J. Janssen[9,10], Rachel Brody[11], Kenneth Palmer[2,12], Silvia M. Uriarte[13], Patrick Ten Eyck[8], David K. Meyerholz[14], Michael L. Merchant[15], Kenneth McLeish[15], Tom Gallagher[4], Jiapeng Huang[16]*, Jun Yan[1,5]*, Stanley Perlman[3]*

[1]Department of Microbiology and Immunology, [2]Center for Predictive Medicine, [5]Division of Immunotherapy, the Hiram C. Polk, Jr., MD, Department of Surgery, Immuno-Oncology Program, Brown Cancer Center, [6]Functional Immunomics Core, Brown Cancer Center, [12]Department of Pharmacology and Toxicology, [13]Department of Oral Immunology and Infectious Diseases, [15]Department of Medicine, Division of Nephrology and Hypertension, [16]Department of Anesthesiology and Perioperative Medicine, University of Louisville, Louisville, Kentucky, 40402, USA

[3]Department of Microbiology and Immunology, [8]Institute for Clinical and Translational Science, [14]Department of Pathology, University of Iowa, Iowa City, Iowa, 52242, USA

[4]Department of Microbiology and Immunology, Loyola University Chicago, Maywood, IL 60153, USA

[7]BIOAGE Labs, Richmond, CA 94804, USA

[9]Department of Medicine, Division of Pulmonary and Critical Care, National Jewish Health, Denver, Colorado, USA.

[10]Department of Medicine, Division of Pulmonary Sciences and Critical Care Medicine, University of Colorado, Aurora, Colorado, USA.

[11]Department of Pathology, Molecular and Cell based Medicine, Icahn School of Medicine at Mount Sinai, New York NY USA.

*Corresponding authors: Stanley Perlman, 51 Newton Rd, Iowa City, IA, 52242, USA. Tel: 319-335-8549. Email: stanley-perlman@uiowa.edu;

Jun Yan, 505 S Hancock St, Louisville, KY, 40245, USA. Tel: 502-852-3628, Email: jun.yan@louisville.edu;

Jian Zheng, 505 S Hancock St, Louisville, KY, 40245, USA. Tel: 502-852-5488, Email: jian.zheng.1@louisville.edu;

32   Jiapeng Huang, 200 Abraham Flexner Way, Louisville, KY, 40202,

33 USA. Tel: 502-569-7983. Email: jiapeng.huang@louisville.edu

36

37 **Abstract**

38 Neutrophils, particularly low-density neutrophils (LDNs), are believed to contribute to acute

39 COVID-19 severity. Here, we showed that neutrophilia can be detected acutely and even months

40 after SARS-CoV-2 infection in patients and mice, while neutrophil depletion reduced disease

41 severity in mice. A key factor in neutrophilia and severe disease in infected mice was traced to the

42 chemokine CXCL12 secreted by bone marrow cells and unexpectedly, endothelial cells. CXCL12

43 levels were negatively correlated with LDN numbers in longitudinal analyses of patient blood

44 samples. CXCL12 blockade in SARS-CoV-2-infected mice increased blood/lung neutrophil

45 numbers thereby accelerating disease progression without changing lung virus titers. The

46 exaggerated mortality caused by CXCL12 blockade can be reversed by neutrophil depletion. In

47 addition, blocking interactions between SARS-CoV-2 and Angiotensin-Converting Enzyme 2

48 (ACE2) reduced CXCL12 levels, suggesting a signal transduction from virus-mediated ACE2

49 ligation to increased CXCL12 secretion. Collectively, these results demonstrate a previously

50 unappreciated role of CXCL12 in diminishing neutrophilia, including low density neutrophilia,

51 and its deleterious effects in SARS-CoV-2 infections. The results also support the involvement of

52 SARS-CoV-2-endothelial cell interactions in viral pathogenesis.

Introduction

SARS-CoV-2, the etiological agent of COVID-19, causes respiratory disease of varying severity, ranging from asymptomatic infection to death (1). Severe disease, which includes hospitalization, ICU admission and death, is characterized by a dysfunctional immune response (2, 3), which is correlated with a poor type 1 interferon response in some patients (4). More generally, these patients demonstrate a prolonged innate immune response, with elevated levels of a group of pro-inflammatory mediators, including IL-6 (5). Notably, severe COVID-19 is often associated with elevated neutrophil counts in the blood (6, 7), and this is often accompanied by lymphopenia (8). Within the increased circulating neutrophil population in SARS-CoV-2 infected patients, a subset of low-density neutrophils (LDNs) ($CD11b^+CD66b^+CD16^{int}$) is specifically increased (9). These cells were initially identified in patients with systemic lupus erythematosus, using Ficoll-Hypaque gradient centrifugation (10) and their appearance was stress-related (11). Unlike mature neutrophils, they have the same density as mononuclear cells after density centrifugation. This LDN subset expresses high levels of pro-inflammatory cytokines and chemokines upon stimulation, likely contributing to the inflammatory milieu in SARS-CoV-2 infected patients (12-14). Functionally, LDNs from COVID patients showed impaired respiratory burst activity and degranulation, indicative of an immature functional phenotype (15). Previous studies have also identified immature LDNs in circulation and lungs of COVID-19 patients (16-20), indicating that severe COVID-19 is associated with the emergence of less mature LDN populations in the circulation and in the bronchoalveolar lavage fluid (BALF), likely due to emergency myelopoiesis (21). In support of this, other reports showed that aging enhances emergency myelopoiesis (22-24). Together these results suggest that during stress, such as severe infection, increased numbers of immature neutrophils are expected. Additionally, LDN activation leads to abundant neutrophil extracellular trap (NET) formation, which is associated with COVID-19 progression (25, 26). Of note, LDNs are immunosuppressive in some settings and include granulocytic myeloid-derived suppressor cells (G-MDSC). G-MDSC were identified in patients with COVID-19 (18, 27). Neutrophilia persists in some COVID-19 survivors, suggesting a possible relationship to PASC (Post-acute Sequelae of COVID-19)(25, 28). Although mechanistic studies are difficult or impossible to perform in patients, the basis and functional relevance of neutrophilia can be addressed in experimentally infected animals, despite differences between human and murine neutrophils (29).

84

85   Mice, hamsters, and nonhuman primates are susceptible to SARS-CoV-2 infection (30-33).

86   Mice are not susceptible to infection with ancestral strains of SARS-CoV-2, although they can be

87   infected with many recent variants (34). The incompatibility between mouse ACE2 (mACE2) and

88   the ancestral SARS-CoV-2 spike (S) glycoprotein is rectified by one or two amino acid changes

89   in the S protein or in mACE2. Therefore, we and others developed mouse-adapted versions of the

90   ancestral strain by mutating the spike protein (13, 32, 35). To generate a virulent mouse-adapted

91   SARS-CoV-2, we inserted the N501Y mutation into the SARS-CoV-2 genome using reverse

92   genetics and passaged this mutant virus through mouse lungs (32). After 30 passages, the virus

93   (SARS2-N501Y$_{MA30}$) became highly virulent such that 5000 pfu caused lethal disease in young

94   BALB/c mice. SARS2-N501Y$_{MA30}$ infection resulted in age-dependent pathogenesis in

95   C57BL/6N mice, similar to the age dependence observed in patients.

96

97   The present study used a cohort of COVID-19 patients and a mouse model of COVID-19 in

98   which middle-aged (8-10-month-old) mice were infected with SARS2-N501Y$_{MA30}$ to examine the

99   role of LDNs in acute COVID-19 and the persistence of neutrophilia after recovery from acute

100   infection. We confirmed the presence of neutrophilia and increased LDNs in COVID-19 patients

101   and infected mice and showed that they also persisted for months after acute infection. We

102   identified a critical role for a single chemokine, CXCL12, in controlling neutrophilia in mice.

103   Additionally, increased plasma CXCL12 levels correlated with decreased numbers of circulating

104   LDNs in a subset of COVID-19 patients who ultimately survived their disease.

Results

Neutrophilia with increased LDNs is present in acutely ill and convalescent COVID-19 patients.

Previous studies showed that LDNs are markedly expanded in some COVID-19 patients (9), and we reported that a subset of LDNs with intermediate CD16 expression (CD16^{int}) is associated with disease severity and worse clinical outcomes (9). Although the presence of CD16^{int} LDNs in bronchoalveolar lavage fluid suggests they are recruited to the lungs in severe COVID-19, this LDN recruitment has not been directly demonstrated. Imaging mass cytometry analysis of lung tissue obtained from 5 COVID-19 patients (Patient data in Table 1) at autopsy revealed extensive infiltration of LDNs (CD11b^{+}CD66b^{+}CD16^{int}) into the lung parenchyma (Figure. 1A). Additionally, the increased number of CD66b^{+}CD15^{+}CD16^{int} LDNs in peripheral blood of COVID-19 patients correlated with the disease severity (Figure. 1B, Patient data in Table 2). Therefore, we interpreted these data to indicate that a distinct LDN subset is recruited from the circulation into lung parenchyma in severe COVID-19.

To determine whether blood total LDN numbers return to normal levels after the acute phase, a separate cohort of convalescent COVID-19 patients were recruited at times ranging from 1 month to 13 months after hospital discharge (Patient data in Table 3). We found that LDNs continued to be present in the peripheral blood with higher numbers in convalescent patients than in age-matched healthy donors (Figure. 1C and D). In addition, LDN frequencies were lower with time from discharge (Figure. 1E). Thus, persistently activated LDNs are present in convalescent patients, although their numbers wane over time, implying their potential contribution to PASC.

LDNs from COVID-19 patients show distinct protein expression profiles compared to normal-density neutrophils (NDNs) that may contribute to more severe disease.

We previously reported that peripheral blood LDNs from severe COVID-19 patients show enhanced NET formation and cytokine production, but impaired degranulation and priming of phagocytosis and respiratory burst activity, compared to NDNs (9, 15). LDNs from COVID-19 patients also showed enhanced interaction with platelets, while these platelets may be potently activated by CD16^{int} LDNs. To further establish differences between peripheral blood neutrophil subsets from COVID-19 patients, proteomic analysis (Figure. 1F and G) was performed on NDNs and LDNs isolated from 13 patients exhibiting increased LDNs from a second cohort of hospitalized COVID-19 patients. Following quantitation of peptides identified by mass

6

136 spectrometry using Scaffold, a total of 1830 proteins were identified. As shown in a volcano plot

137 (Figure. 1F), 326 proteins exhibited significantly greater expression in NDNs, while 134 proteins

138 exhibited greater expression in LDNs. The comparison of the protein expression pattern of LDNs

139 and NDNs indicates distinctly different expression patterns by the two neutrophil subsets (Figure.

140 1G). The ten most significant Gene Ontology Biological Processes represented by proteins with

141 significantly different expression between NDNs and LDNs are listed in Table 4. NDNs show

142 enhanced expression of proteins involved in leukocyte activation and degranulation. On the other

143 hand, proteins with increased expression by LDNs are involved in regulation of coagulation and

144 complement activation. Analysis of these data revealed that CD16^{int} LDN expressed higher levels

145 of proteins corresponding to gene markers of immature neutrophils and lower levels of proteins

146 associated with mature circulating neutrophils (Figure 1F and G). These results are consistent with

147 bulk RNAseq data showing that CD16^{int} LDN from COVID-19 patients exhibit higher expression

148 levels of gene markers associated with immaturity compared to CD16^{hi} LDN (9).

149

150 *Levels of plasma CXCL12 negatively correlated with percentage of peripheral blood LDNs.*

151 Although chemokines responsible for recruiting neutrophils to infected lungs, such as CXCL9,

152 CXCL10, and CCL5, have been well studied (9, 36), whether some chemokines may provide

153 negative feedback by regulating the distribution of inflammatory neutrophils remains poorly

154 understood. The CXCR4-CXCL12 axis has important roles in the migration and distribution of

155 neutrophils (37), including retention of immature neutrophils in the bone marrow prior to release

156 into the circulation (38) and recruitment of apoptotic neutrophils into the bone marrow for

157 destruction by macrophages (37-39). Because of these important roles for CXCL12 in neutrophil

158 trafficking, we next assessed whether CXCL12 levels were related to alterations in CD16^{int} LDN

159 dynamics in SARS-CoV-2-infected patients, utilizing a previously described cohort of

160 hospitalized COVID-19 patients (9). Serial peripheral blood samples collected at multiple time

161 points after admission from 24 patients were used to determine the percentages of peripheral blood

162 CD16^{int} LDNs by CyTOF and plasma concentrations of CXCL12 by ELISA. In this cohort, 6 of

163 15 survivors showed a negative correlation between the percentages of peripheral blood CD16^{int}

164 LDNs and plasma concentrations of CXCL12 during hospitalization (Figure. 2A and B). The other

165 9 survivors had neither increased numbers of blood LDNs (9) nor elevated CXCL12 levels

166 (Supplemental Figure. 1), making it impossible to carry out correlative analysis of the percentage

167 of CD16^{int} LDNs and plasma CXCL12 levels. It is possible that these 9 patients were enrolled after

168 their LDN levels peaked, during the period when CXCL12 levels had already declined. In contrast,

169 all 9 deceased patients showed increased CD16^{int} LDNs, and the correlation between the

170 percentage of CD16^{int} LDNs and CXCL12 levels was close to zero (p =0.91) (Figure. 2C and D).

171 These results suggest that the initial recruitment of LDNs was critical for inducing CXCL12 while

172 the late accumulation of LDN in deceased patients failed to trigger CXCL12 production. Together,

173 these data are consistent with the notion that CXCL12 regulates CD16^{int} LDN accumulation in the

174 circulation of COVID-19 survivors who have elevated numbers of CD16^{int} LDNs. As LDNs

175 account for a substantial portion of neutrophils in the lung parenchyma, these findings support the

176 conclusion that CXCL12 plays a regulatory role in COVID-19 immunopathogenesis.

177

178 *Neutrophilia contributes to disease severity of SARS2-N501Y$_{MA30}$-infected mice.*

179 While these patient data are consistent with a role for LDNs in disease severity and for CXCL12

180 in protection, further mechanistic studies are difficult without a robust experimental model of

181 COVID-19 infection. To develop such a system for studying acute and prolonged neutrophilia, we

182 infected middle-aged (8-10-month-old) C57BL/6N mice intranasally with 1000, 2000, or 5000 pfu

183 SARS2-N501Y$_{MA30}$ to determine the optimal sublethal dose. Mice exhibited dose-related disease

184 severity, characterized by weight loss, increased mortality, and elevated lung viral titers (Figure.

185 3A-C). In contrast, young (8-10-week-old) C57BL/6N mice did not succumb to challenge with the

186 same doses of SARS2-N501Y$_{MA30}$ (Supplemental Figure. 2), mimicking the response observed in

187 a majority of young SARS-CoV-2-infected patients.

188 Neutrophil activation/dysregulation, characterized by secreted NETs and pro-inflammatory

189 cytokines/chemokines is common in severe COVID-19 cases (9, 21, 40). Consistent with this

190 human condition, numbers of neutrophils in peripheral blood (Figure. 3D and E) and lungs (Figure.

191 3F and G) in SARS2-N501Y$_{MA30}$-infected mice (neutrophil gating strategies are shown in

192 Supplemental Figure. 3A) correlated with acute weight loss. Further, neutrophils were recruited

193 into the lung parenchyma of mice with severe COVID-19, analogous to the human infection

194 (Figure. 3H). In support of the pathogenic role of neutrophils in acute SARS2-N501Y$_{MA30}$

195 infection, neutrophil depletion by anti-Ly6G antibody ameliorated weight loss and improved

196 survival (Supplemental Figure. 3B and C, Figure. 3I-L). The anti-Ly6G treatment was therapeutic

197 despite having no direct antiviral activity, as measured by lung virus titers (Figure. 3M).

8

198

LDN subset numbers correlate with infected mouse disease severity.

To determine the contribution of specific neutrophil subsets to the pathogenesis of acute COVID-19, flow cytometry was used to identify immature ($CD15^+CD16^+CD115^-CXCR2^-$), mature ($CD16^{hi}CD62L^{hi}CXCR2^{hi}CXCR4^{low}$), senescent ($CD11b^{hi}CXCR2^{low}CD62L^{low}CXCR4^{hi}$), degranulated ($CD11b^+CD18^+Gr-1^{int}$) neutrophils, and LDNs (mouse LDNs are $ARG1^+CD15^+CD33^+CD101^-CXCR4^+$) [41] in the peripheral blood of middle-aged mice infected with 5000 pfu of SARS2-N501Y$_{MA30}$ (Gating strategies are shown in Supplemental Figure. 4A)[41]. As summarized in Figure. 4A, the percentage and the number of immature neutrophils and LDNs, but not mature neutrophils, in peripheral blood increased substantially in mice at day 5 post infection compared to mock-treated mice. Importantly, only the increased numbers of LDNs in peripheral blood (Figure. 4B) and lungs (Figure. 4C) correlated with weight loss. Furthermore, neutrophilia and increased LDNs persisted as long as 90 dpi in middle-aged mice, long after mice recovered from severe disease (Figure. 4D and E). Thus, SARS-CoV-2 infection in mice recapitulated the increase in circulating LDNs and recruitment of LDNs into lung parenchyma observed in humans. Taken together, the amelioration of disease by neutrophil depletion in infected mice and the correlation of LDNs in the circulation and lungs with disease activity suggest that LDNs make a substantial contribution to the severity of COVID-19.

CXCR4-CXCL12 regulates the accumulation of peripheral blood LDNs.

Since the clinical data in Figure. 2 suggested an important role for CXCL12 in regulating LDNs in the blood and lungs, we further investigated factors important for neutrophil trafficking using SARS2-N501Y$_{MA30}$-infected mice. We focused on chemokine/cytokine levels in the blood and lungs. In SARS-CoV-2-infected patients, several molecules were shown to be positively correlated with LDN numbers (CXCL10 in the BALF and IL-10, IL-1R, MCP-1, MIP-1 in the plasma)[9]. In contrast, CXCL12 was the sole chemokine in infected mice that correlated negatively with numbers of LDNs, while no chemokines were positively correlated (no significant associations were found between the levels of CXCL1, CXCL2, CXCL9, CXCL10, CCL2, CCL3, and CCL5 and LDN numbers). To further investigate the role of CXCL12 in LDN numbers, we measured plasma CXCL12 levels and assessed CXCR4 expression on neutrophils and CD4 and CD8 T cells in middle-aged mice infected with 5000 pfu of SARS2-N501Y$_{MA30}$. Peripheral LDN numbers

decreased as plasma CXCL12 levels increased, whereas no correlation was identified with other neutrophil subsets or CD4/8 T cells (Figure. 5A). Compared to other neutrophil subsets and CD4 and CD8 T cells, LDNs expressed higher levels of CXCR4 (Figure. 5B).

To identify the cellular origin of CXCL12, intracellular CXCL12 levels in peripheral blood and lung cell subsets, and in vascular endothelial cells (Figure. 5C and D, Supplemental Figure. 4B), were determined by flow cytometry. The highest levels of CXCL12 were detected in vascular endothelial cells and lung macrophages (Figure. 5C and D, Supplemental Figure. 4B). CXCL12 mRNA was significantly increased only in endothelial cells after infection, indicating that endothelial cells may be a source of plasma CXCL12 (Supplemental Figure. 4C) and not just serve as 'sinks' for circulating CXCL12. The increased CXCL12 in endothelial cells may keep circulating LDNs from infiltrating into lung parenchyma. As the bone marrow is a major source of CXCL12 in both homeostatic and pathological settings (42), CXCL12 RNA and protein expression in bone marrow from infected mice were measured by real-time quantitative polymerase chain reaction (RT-qPCR) and ELISA, respectively. CXCL12 mRNA in bone marrow homogenates increased after SARS2-N501Y$_{MA30}$ infection, while protein levels of CXCL12 failed to increase (Figure. 5E). The discrepancy between mRNA and protein levels of soluble factors is common and may be derived from diverse causes (43-45). Considering the increased plasma CXCL12, we speculate that the discrepancy of bone marrow CXCL12 mRNA and protein level could be due to its rapid binding to receptors or equilibration between bone marrow and blood. Thus, the bone marrow is likely also a site of CXCL12 production in infected mice, as previously reported (42). Together, these results suggest that CXCR4-CXCL12 interactions reduce lung infiltration by neutrophils by directing them to the vasculature and bone marrow, thereby diminishing the pathogenic effects of neutrophils.

CXCL12 blockade enhances disease progression in SARS2-N501Y$_{MA30}$-infected mice by regulating neutrophil distribution.

To determine whether CXCL12 protects mice from disease progression, middle-aged C57BL/6N mice infected with a sublethal dose (1000 pfu) of SARS2-N501Y$_{MA30}$ were treated with anti-CXCL12 antibody or isotype control (Figure. 6A). Anti-CXCL12 antibody treatment reduced CXCL12 levels in the blood but did not diminish levels of CXCL12 protein in endothelial cells (Supplemental Figure. 5C and D), consistent with the notion that endothelial cells are a source for

260   CXCL12 and do not function only to remove it from the blood. Further, CXCL12 blockade
261   increased mortality (Figure. 6B) and lung histopathology scores (Figure. 6C) of SARS2-
262   N501Y$_{MA30}$-infected mice but did not change lung virus titers (Figure. 6D).

263   Consistent with its pathogenic effects, anti-CXCL12 antibody treatment (Figure. 6E) resulted
264   in increased accumulation of neutrophils in peripheral blood and lungs of infected mice (Figure.
265   6F). This was likely due to reduced CXCL12-mediated sequestering of neutrophils in the bone
266   marrow and, perhaps, enhanced neutrophil attachment to vascular endothelium. Next, we tracked
267   peripheral neutrophil distribution after they were labeled intravenously with CFSE (Figure. 6E).
268   The numbers of CFSE$^+$ neutrophils increased in the lung but decreased in bone marrow after anti-
269   CXCL12 antibody treatment (Figure. 6G), suggesting decreased recruitment back to the bone
270   marrow (Figure. 6F). To directly assess the role of neutrophils in anti-CXCL12 enhanced disease,
271   we treated SARS2-N501Y$_{MA30}$-infected mice with anti-CXCL12 antibody, in conjunction with
272   anti-Ly6G antibody or its isotype control (Figure. 6H). Depletion of neutrophils rescued most mice
273   from mortality caused by CXCL12 blockade (Figure. 6I), consistent with a role for CXCL12 in
274   ameliorating immunopathology by regulating the distribution of neutrophils, especially LDNs.
275   Notably, at the dose of virus used in these experiments, no mice died. Therefore, neutrophil
276   depletion would not be expected to improve outcomes in the absence of anti-CXCL12 antibody
277   treatment.

278   Of note, CXCL12 blockade had no effects on the numbers of neutrophil progenitor cells in the
279   bone marrow (hematopoietic stem cells (HSC), common myeloid precursors (CMP), granulocyte-
280   monocyte progenitor (GMP)) (Supplemental Figure. 6A and B). Finally, recombinant mouse
281   CXCL12 administered intravenously modestly ameliorated disease severity (Supplemental Figure.
282   6C-E). Survival of mice was slightly prolonged with differences trending towards statistical
283   significance (Supplemental Figure. 6E). Based on the results described above, effects on clinical
284   disease would be expected to be greater if CXCL12 was targeted directly to the bone marrow or if
285   a stabilized form was available (necessary because rodent CXCL12 has a half-life of
286   approximately 26 minutes) (46).

287

288   *CXCL12 blockade does not affect adaptive immune responses in SARS2-N501Y$_{MA30}$-infected mice.*
289   CXCL12 is known to affect T cell trafficking (47), so we also examined whether CXCL12
290   blockade affected the generation of virus-specific neutralizing antibody or T cell responses

11

291   (Supplemental Figure. 7A). Virus-specific T cell responses were measured directly ex vivo by

292   stimulating cells with SARS-CoV-2 peptide pools (spike protein, membrane protein, and

293   nucleoprotein peptide pools). As shown in Supplemental Figure. 7B-D, no significant differences

294   were found in numbers of total T cells or levels of neutralizing antibody in mice receiving anti-

295   CXCL12 antibody or control treatment. Moreover, CXCL12 blockade did not affect the

296   development of virus-specific memory CD4 and CD8 T cell responses in the blood or lungs when

297   assessed at day 30 after SARS2-N501Y$_{MA30}$ infection (Supplemental Figure. 7E and F). CXCL12

298   treatment increased the numbers of blood neutrophils and LDNs but did not affect the distribution

299   of T cell subsets in naïve mice (Supplemental Figure. 7G and H). These results are not unexpected

300   because CXCR4 levels were much lower on T cells than neutrophils (Figure. 5B) and there was

301   no correlation between CXCL12 concentration and T cell numbers (Figure. 5A). To further

302   confirm that T cells were relatively unresponsive to modulation of the CXCR4-CXCL12 axis, we

303   treated middle-aged mice with extremely high doses of anti-CXCL12 antibody (100mg/kg). As

304   shown in Supplemental Figure. 7I and J, high doses of anti-CXCL12 antibody modestly decreased

305   the number of CD4/CD8 T cells in naïve mice but had no effect in SARS-CoV-2-infected mice.

306   Moreover, to confirm the specificity of the anti-CXCL12 blocking antibody, we assessed its

307   binding to CXCL12 protein. As shown in Supplemental Figure. 8, the blocking antibody bound

308   equivalently as antibody used in ELISA to CXCL12 protein. These data collectively indicated that

309   T cell migration is slightly altered upon CXCL12 blockade, but much higher antibody doses were

310   required compared to the level needed to impact neutrophil trafficking.

311

312   *CXCL12 expression by endothelial cells is SARS-CoV-2 specific and involves ACE2 binding.*

313   Endothelial cell CXCL12 mRNA and protein upregulation by SARS-CoV-2 infection was

314   unexpected, so we next assessed whether this upregulation was a generalized response to

315   respiratory virus infection. We infected mice with SARS2-N501Y$_{MA30}$ or two other pathogenic

316   human respiratory viruses, influenza A virus (IAV-PR8) and mouse-adapted MERS (Middle East

317   respiratory syndrome)-CoV (MERS$_{MA}$)(48) with virus doses that resulted in equivalent clinical

318   disease (Figure. 7A). SARS-CoV-2, but not IAV-PR8 or MERS$_{MA}$, infection induced significantly

319   increased numbers of neutrophils and LDNs in the blood (Figure. 7B and C). Meanwhile, CXCL12

320   expression in endothelial cells was increased only after infection with SARS-CoV-2 (Figure. 7D-

321   G). This result raised the possibility that SARS-CoV-2 interactions with ACE2 on endothelial cells

322   (48) was critical for increased CXCL12 expression by these cells. To assess this possibility, we

323   engineered SARS-CoV-2 receptor binding domain (RBD) conjugated to a stabilizing

324   immunoglobulin Fc (SARS-2-RBD-Fc), and, as a control MERS-CoV (EMC/2012) S protein

325   NTD (N terminal domain)-Fc. As shown in Figure. 7E, H and I, treatment with MERS-CoV S

326   NTD-Fc or SARS-2-RBD-Fc from ancestral strains of SARS-CoV-2, which cannot bind to

327   mACE2, had no effect, whereas treatment with low amounts of SARS-2 (N501Y) RBD-Fc, which

328   can bind to mACE2, resulted in CXCL12 downregulation in endothelial cells. Of note, only high

329   amounts of SARS-2 (N501Y) RBD-Fc prolonged survival, probably by more effectively blocking

330   virus entry into susceptible cells.

Discussion

Here we show that neutrophilia and increased levels of LDNs, characteristic manifestations of severe COVID-19, are also observed in mice infected with SARS-CoV-2. Of note, we observed the benefits of neutrophil depletion in mice with severe disease, which is contrast to a previous report showing no effect of depletion in mice with mild disease (49), suggesting the role for neutrophils mainly in severe disease. Consistent with their increased number in peripheral blood (9), LDNs represent the major neutrophil population accumulating in the lung parenchyma of patients with severe COVID-19 (Figure. 1A). In addition, LDNs expressed increased levels of proteins that are associated with complement and coagulation cascades (Figure. 1F and G, Table 4), suggesting a critical role of LDNs in SARS-CoV-2-related inflammation and thrombosis. More importantly, consistent with observations made on patient samples (9), numbers of LDNs were increased in SARS-CoV-2 infected mice and their number correlated with clinical disease severity (Figure. 4B and C).

Plasma CXCL12 is the ligand for CXCR4, is upregulated in COVID-19 (50) and has been shown to be a marker for disease severity (51). Polymorphisms in CXCL12 were shown to correlate with disease severity, emphasizing the importance of this chemokine (52). CXCR4 expression on LDNs (Figure. 5B) enhanced their migration to sites of CXCL12 production. Our results further demonstrate the protective role of CXCL12 in SARS-CoV-2 infection in mice (Figure. 6B-D). Notably, the negative correlation in the blood and lungs between LDN numbers and CXCL12 expression (Figure. 4C and 5A) was also observed in COVID-19 survivors (Figure. 2A and B). To our best knowledge, no other chemokine or cytokine levels negatively correlated with LDN numbers to the same extent in patient plasma, although other molecules, such as GM-CSF are upregulated in patients with severe COVID-19 and could contribute to neutrophilia (53).

Strikingly, upregulation of CXCL12 expression by endothelial cells is observed specifically in murine infection with SARS-CoV-2 but not after influenza A virus or MERS-CoV infection (Figure. 7E-G). Endothelial cells are known to express ACE2 (54), and endothelial dysfunction is a well described characteristic of SARS-CoV-2 infection (55). While endothelial cells do not appear to be productively infected by SARS-CoV-2, infectious virus is required for increased CXCL12 expression; SARS-2 (N501Y) RBD-Fc by itself does not result in enhanced CXCL12 expression (Figure. 7D). CXCL12 expression by endothelial cells could result from direct interactions with virus, or indirectly through virus-ACE2 interactions on other cells, with

362 subsequent effects on endothelial cells. SARS-CoV-2 binding to ACE2 may interfere with normal

363 ACE2 function, resulting in activation of NF-kB and increased production of pro-inflammatory

364 molecules (56). These data suggest that, in addition to limiting neutrophil egress from the bone

365 marrow (57), CXCL12-CXCR4 interactions protect against lung injury in SARS-CoV-2 infections

366 by regulating neutrophil trafficking into the lungs. These effects on trafficking are abrogated after

367 treatment with anti-CXCL12 antibody (Figure. 6F and G), resulting in increased numbers of LDNs

368 in the lungs and clinical deterioration. Further work will be required to determine the relative

369 importance of CXCL12 expression by bone marrow vs. endothelial cells in regulating the

370 dynamics of LDNs and other immune cells. In addition, monocytes, dendritic cells (DCs) and

371 neutrophils also expressed CXCL12 albeit at substantially lower levels than endothelial cells

372 (Figure. 5D), which could also contribute to elevated CXCL12 levels in the blood. Although

373 CXCL12 is expressed by alveolar epithelial cells (58), increased LDN recruitment into the lungs

374 after CXCL12 blockade suggests that LDNs migrate to the lung in response to other

375 chemoattractants, such as CXCL1, CCL2 and CXCL10, expressed in the infected lung (36). It is

376 also noteworthy that lung-recruited neutrophils were also found to contribute to the pathogenesis

377 of influenza A virus infection (59, 60). Although IAV-PR8 infection failed to increase blood

378 neutrophil numbers or CXCL12 expression by endothelial cells (Figure. 7B-D), the involvement

379 of the CXCL12-CXCR4 axis in regulating neutrophil, especially LDN, accumulation in the lungs

380 and bone marrow deserves further investigation.

381   Additionally, we show that neutrophilia persists in mice that survive SARS-CoV-2 infection

382 (Figure. 4D and E). Long term effects of SARS-CoV-2, including lung fibrosis,

383 neuroinflammation and behavioral changes, are apparent in previously infected hamsters and mice

384 (61-63), and neutrophilia could contribute to these sequelae. These results mirror clinical

385 observations that neutrophilia persists for several months in patients after resolution of acute

386 SARS-CoV-2 infection (64) (Figure. 1C-E). Increased expression of mRNAs and proteins

387 associated with neutrophil-mediated inflammation was detected in COVID-19 patients with

388 persistent lung changes at 3-12 months after infection (25). Changes in markers indicative of

389 increased NETs formation were identified in these patients. Extracellular newly identified receptor

390 for advanced glycation end-products binding protein (EN-RAGE), expressed by LDNs in COVID-

391 19 patients (18), and the chemokine IL-17C, important for neutrophil migration (65), were also

392 expressed at higher levels in COVID-19 survivors with interstitial/fibrotic pulmonary disease.

393   LDN numbers correlated with more severe disease in patients with acute COVID-19 (9, 18, 21),
394   as well as in other conditions, including sepsis (66). In most settings, LDNs are pro-inflammatory
395   and have decreased chemotactic ability, decreased phagocytic activity and increased expression of
396   pro-inflammatory molecules, similar to the LDNs that we identified (Figure. 1F and G, Table 4).
397   There are limitations with these studies. First, it will be critical to specifically deplete LDNs in
398   mice and assess effects on clinical disease. No useful antibody or other method for depleting LDNs
399   is now available, making these experiments impossible. Second, our data show that CXCL12 had
400   important effects on neutrophils, particularly LDN trafficking in SARS-CoV-2 infections.
401   However, in the absence of biomarkers specific for LDNs, the role of CXCL12-CXCR4 signaling
402   in LDN trafficking is not fully proven. Meanwhile, CXCR12-CXCR4 signaling appears to have
403   different roles in different clinical settings and is difficult to precisely define, partly because
404   CXCL12 null mice are not viable (67, 68). Thus, CXCL12 blockade or conditional CXCL12
405   knock-out in tumors (69, 70) and neuroinflammatory disease models (71-73) has led to
406   contradictory conclusions, suggesting that the role of CXCL12-CXCR4 signaling is disease
407   context-dependent. Given the pleiotropic effects of CXCL12, it will also be important to extend
408   these analyses to studies of the role of CXCL12 in trafficking of other immune cells such as NK
409   cells and pDCs in infected mice.
410   Collectively, our results show that neutrophilia can persist for extended periods of time after
411   resolution of acute SARS-CoV-2 in infected mice and patients. Decreases in LDN numbers, which
412   contributes to disease resolution in mice, are dependent upon interactions between CXCL12 and
413   CXCR4. These data support the value of measuring CXCL12 levels to predict disease severity and
414   long-term sequelae of COVID-19 infections and identify it as a possible target for therapeutic
415   intervention.

Methods

Sex as a biological variant.

In preliminary experiments, we did not observe significant differences between male and female mice. Consequently, equal numbers of male and female mice were used in these studies.

Study participants and clinical data

Inclusion criteria were all hospitalized adults (older than 18) who had positive SARS-CoV-2 results and consented to this study. Exclusion criteria included age younger than 18 or refusal to participate. Patients enrolled in this study were diagnosed with a RT-qPCR-based 2019-CoV detection kit at the University of Louisville hospital laboratory using nasopharyngeal swab samples obtained from patients. All patients with acute SARS-CoV-2 infection were followed by the research team daily, and the clinical team was blinded to findings of the research analysis to avoid potential bias. Demographic characteristics (age, sex, height, weight, BMI, and clinical data: symptoms, comorbidities, laboratory findings, treatments, complications, and outcomes) were collected prospectively. The infected patients described in Figure. 2 were previously reported (9).

Virus

SARS2-N501Y$_{MA30}$ and MERS$_{MA}$ were generated as described previously (32, 74). Mouse-adapted IAV A/PR/8/34 (IAV-PR8) was a gift from K. Legge (Department of Pathology, University of Iowa).

Mice

8-10-week-old or 8-10-month-old male and female C57BL/6N mice were obtained from Charles River Laboratories. *hDPP4*-KI mice were developed and propagated as described previously (74). Mice were maintained in the Animal Care Unit at the University of Iowa and Regional Biocontainment Laboratory (RBL) at the University of Louisville under standard conditions of dark/light cycle, ambient temperature, and humidity. Mice were randomly assigned to different groups, with numbers per group sufficient to obtain statistical significance.

Mouse infection

446 In most experiments, mice were infected lethally (5000 pfu) or sublethally (1000 or 2000 pfu) with

447 SARS2-N501Y$_{MA30}$. Some mice were infected sublethally with 500 pfu influenza A virus-PR8

448 (IAV-PR8) or 500 pfu mouse-adapted MERS-CoV (MERS$_{MA}$). Animal weight and health were

449 monitored daily. All experiments with SARS-CoV-2 and MERS$_{MA}$ were performed in a Biosafety

450 Level 3 (BSL3) Laboratory at the University of Iowa and the University of Louisville. Experiments

451 with IAV-PR8 were performed in a BSL2 Laboratory at the University of Louisville.

452

453 *Plasma and PBMC isolation*

454 Whole blood samples of patients were centrifuged at 541×g for 10 minutes. Plasma and PBMCs

455 were processed as described previously (9).

456

457 *Human lung slides preparation and imaging mass cytometry*

458 Lung tissue sections from deceased COVID-19 patients were stained with metal-labeled

459 antibodies. Anti-CD66b (BLR11H)-166Er, Cat# 91H033166, 1:150; anti-CD16 (EPR16784)-

460 149Sm, Cat# 91H004149, 1:150; anti-collagen (polyclonal)-142Nd, Cat# 91H018142, 1:300; anti-

461 αSMA (1A4)-153Eu, Cat# 91H001153, 1:300 and anti-Pan-Cytokeratin (AE-1/AE3)-174Yb, Cat#

462 91H006174, 1:200 was purchased from Standard BioTools. Purified anti-CD15 (W6D3)

463 (Biolegend, Cat# 323035) and anti-SARS-CoV-2 Spike S1 subunit (R&D, Cat# MAB105407)

464 were labelled with 172Yb and 173Yb at 1:100 and 1:200 dilutions, respectively (Maxpar® X8

465 Multimetal Labeling Kit, Cat# 201300, Standard BioTools). All antibodies were first validated to

466 confirm optimal staining intensity, specificity, and signal-to-noise ratio. Stained tissue sections

467 were ablated by using the Hyperion mass cytometry imaging system (Standard BioTools). The

468 Hyperion was autotuned using a 3-element tuning slide (Standard BioTools) as described in the

469 Hyperion imaging system user guide. An extra minimum threshold of 1000 mean duals of 175Lu

470 was used. At least three 2500x1500 μm regions of interest (ROIs) per sample were selected and

471 ablated at 200 Hz. Data were visualized by using MCD viewer software (Standard BioTools). For

472 downstream analysis, image data were exported as tiff.ome files from the MCD viewer, followed

473 by cell segmentation using CellProfiler (developed by Broad Institute of MIT and Harvard, 4.2.1).

474 .fcs files or .cvs files were exported using histoCAT software. The .fcs files were further analyzed

475 using Flowjo software (BD).

476

477 *Synthesis of Fc-recombinant proteins*

478 SARS-2-RBD-Fc and a control construct, MERS (EMC)-NTD-Fc, were synthesized and evaluated

479 previously (75). MERS (EMC)-NTD-Fc contains the MERS-CoV S protein N terminal domain

480 bound to Fc. SARS-2 (N501Y)-RBD-Fc was synthesized following site-directed mutagenesis of

481 the N501 codon within pCEP4-SARS-2-RBD-Fc. The pCEP4 expression plasmids were

482 transfected into HEK293T cells using LipoD (SignaGen, Cat# SL100668). Transfected cells were

483 grown in FBS-free DMEM containing 2% (wt/vol) Cell Boost 5 (HyClone, Cat# SH30865.01).

484 Conditioned media were collected on days 3 and 6 and clarified free of debris (300×g, 4°C, 10 min;

485 4,500×g, 4°C, 10 min). Fc-tagged proteins were purified using HiTrap protein A high-

486 performance columns (GE Healthcare, Cat# GE17-0402-01) according to the manufacturer's

487 instructions. Purified proteins were dialyzed in PBS (pH 7.4), quantified spectrophotometrically,

488 and stored at −20°C until use.

489

490 *Histopathology and scoring*

491 Formalin-fixed paraffin embedded lungs were sectioned (~4 μm) and stained with hematoxylin

492 and eosin (HE). Tissues were evaluated by a board-certified pathologist (DKM) using the post-

493 examination method of masking to groups (76). Edema was ordinary scored (0-4) as previously

494 described (32).

495

496 *Collection of whole blood/serum from mice*

497 Mice were anesthetized by intraperitoneal injection of ketamine-xylazine. Blood was collected

498 through retro-orbital bleed with a capillary tube (Fisher Scientific). Blood was allowed to clot at

499 room temperature for 30 minutes. Sera were clarified by centrifugation and transferred to a new

500 tube for storage at -80°C. For collection of whole blood, heparinized capillary tubes were used

501 (Fisher Scientific).

502

503 *Lung, spleen, bone marrow and abdominal aorta cell preparation*

504 After perfusion, lungs and abdominal aorta of mice were removed, minced, and digested in HBSS

505 buffer consisting of 2% fetal calf serum, 25 mM HEPES, 1 mg/ml collagenase D (Roche) and 0.1

506 mg/ml DNase (Roche) at 37°C for 30 minutes. To collect bone marrow, the ends of femurs were

507 cut and the marrow plug was flushed with 1 ml of complete RPMI 1640 media. Single-cell

508 suspensions of lungs, spleens, bone marrow and abdominal aorta were prepared by passage

509 through a 70 μm cell strainer. Lung macrophages (CD45$^+$CD68$^+$F4/80$^+$) and vascular endothelial

510 cells (CD45$^-$CD31$^+$CD54$^+$) were purified from single-cell suspensions of lungs and abdominal

511 aorta using a BD FACSAria.

512

513 *Flow cytometry*

514 Cells were enumerated with a Scepter 2.0 cell counter (MilliporeSigma), washed and blocked with

515 1 μg α-CD16/α-CD32 antibody (clone 2.4G2, StemCell) at 4 °C for 20 minutes and surface stained

516 with the following antibodies at 4°C for 30 minutes: APC α-mouse CD16/CD32 (clone 2.4G2, BD

517 BioScience); V450 α-mouse CD45 (clone 30-F11); APC α-mouse B220 (clone RA3-6B2);

518 APC/Cyanine 7 α-mouse CD3e (clone 145-2C11); APC/Cyanine 7 α-mouse CD11c (clone FC);

519 FITC or PE or BV21 α-mouse Ly6G (clone 1A8); BV510 or PE α-mouse CD11b (clone M1/70);

520 PE/Cyanine 7 α-mouse CD8 (clone 53-6.7); PerCP/Cyanine 5.5 α-mouse CD4 (clone RM4-5);

521 PerCP/Cyanine 5.5 α-mouse Ly6C (clone HK1.4); PE α-mouse CD 64 (clone X54-5/7.1); BV421

522 α-mouse CD115 (clone AFS98), Alexa Fluor 488 α-mouse CD15 (clone MC480), APC α-mouse

523 CD18 (clone H155-78), APC α-mouse CD31 (clone W18222B), APC α-mouse CD33 (clone

524 W18124D), PE α-mouse CD34 (clone HM34), FITC α-mouse CD54 (clone YN1/1.7.4), Pacific

525 Blue α-mouse CD62L (clone W18021D), PE-Cy7 α-mouse Gr-1 (clone RB6-8C5), PE-Cy7 α-

526 mouse CD68 (clone FA11), PE-Cy7 α-mouse CD93 (clone AA4.1), PE-Cy7 α-mouse CD101

527 (clone Moushi101, Invitrogen), FITC α-mouse CD127 (clone SB/199), BV421 α-mouse CD135

528 (clone A2F10), PE-Cy5.5 α-mouse CXCR2 (clone SA045E1), FITC or PE-Cy5.5 α-mouse

529 CXCR4 (clone L276F12), FITC α-mouse MHC-II (clone 39-10-8), APC α-mouse ARG1 (R&D),

530 Pacific Blue α-mouse F4/80 (clone BM8), BV510 α-mouse Sca-1 (clone D7), APC-Cy7 α-mouse

531 c-kit (clone ACK2). Antibodies were purchased from BioLegend if not specified and were used at

532 1:200 dilution. Cells were fixed and permeabilized with Cytofix/Cytoperm (BD Biosciences).

533 For intracellular cytokine staining (ICS), lymphocytes were cultured in 96-well dishes at 37°C

534 for 5-6 h in the presence of 2 μM peptide pools and brefeldin A (BD Biosciences), labeled for cell-

535 surface markers, fixed/permeabilized with Cytofix/Cytoperm Solution (BD Biosciences) and

536 labeled with PE α-mouse CXCL12 (clone MAB310, R&D), APC α-mouse IFN-γ (clone XMG1.2,

537 BioLegend) and FITC α-mouse TNF (clone MP6-XT22, BioLegend) antibody (1:100 dilution).

538   All flow cytometry data were acquired using a BD FACSVerse and analyzed with FlowJo

539   software.

540

541   *RNA isolation and RT-qPCR*

542   Total RNA was extracted from tissues using TRIzol (Invitrogen) or a Direct-zol RNA Miniprep

543   kit (Zymo Research) according to the manufacturer's protocol. cDNA was prepared and the

544   primers used for cytokine and chemokines were previously reported (65). For detection of

545   CXCL12, the following primers were used:

546   F: 5'-GGAGGATAGATGTGCTCTGGAAC-3'; R: 5'-AGTGAGGATGGAGACCGTGGTG-3'.

547

548   *ELISA*

549   Concentrations of human and mouse plasma CXCL12 were determined by ELISA (Human

550   CXCL12/SDF-1α Quantikine ELISA Kit, DSA00; Mouse CXCL12/SDF-1α Quantikine ELISA

551   Kit, MCX120, R&D) according to the manufacturer's instructions.

552   The binding capability of anti-CXCL12 antibodies (clone MAB310 and MCX120) was determined

553   by ELISA using reagents and standard samples included in the ELISA Kit (MCX120, R&D).

554

555   *CFSE staining and cell tracking*

556   To track the migration of peripheral blood neutrophils, 8-10-month-old C57BL/6N mice were

557   infected with SARS2-N501Y$_{MA30}$ (1000 or 2000 pfu) and treated with 2mg/kg CFSE (Invitrogen)

558   diluted in 0.2 ml PBS at day 2 post infection via tail vein injection. CFSE$^+$ cells in peripheral blood,

559   lung and bone marrow were determined by flow cytometry at the indicated time points.

560

561   *Treatment with anti-Ly6G, anti-CXCL12, and rCXCL12*

562   For neutrophil depletion, infected mice were treated at day 1, 3, 5, 7 after infection with 0.2 ml

563   PBS or 20 mg/kg anti-Ly6G (clone 1A8, Bio X Cell) or its isotype control Ig (rat IgG2a, clone

564   2A3, Bio X Cell) diluted in 0.2 ml PBS. For anti-CXCL12 treatment, mice were treated at day 2

565   and 4 after infection with 0.2 ml PBS, or 25 or 100 mg/kg anti-CXCL12 (clone MAB310, R&D)

566   or its isotype Ig (mouse IgG1, clone MAB002, R&D). For rCXCL12 treatment, mice were treated

567   with 10 mg/kg rCXCL12 (R&D) diluted in 0.2 ml PBS at day 2, 5, 8 after infections. Drugs and

568   PBS were administered via tail vein injection.

569

Whole human blood analysis

571 For whole blood analysis, 150 μl of whole blood was lysed with 2 ml of ACK buffer for 10 minutes.

572 Cells were spun down and washed once with PBS. Cells were then stained with APC-Cy7 viability

573 dye, PeCy7 α-human CD45 (clone 2D1), PE α-human CD66b (clone 6/40c), and APC α-human

574 CD16 (clone 3G8, all from BioLegend) for 30 minutes at 4°C prior to washing and analysis using

575 a FACSCanto (BD Biosciences).

576

CyTOF mass cytometry sample preparation

578 As described previously(9), mass cytometry antibodies were either purchased preconjugated

579 (Standard BioTools) or were conjugated in house using MaxPar X8 polymer kits or MCP9 polymer

580 kits (Standard BioTools) according to the manufacturer's instructions. PBMCs were isolated as

581 described above, stained for viability with 5 μM cisplatin (Standard BioTools) washed and stained

582 with the complete antibody panel for 30 minutes at RT. Cells were fixed in 1.6% formaldehyde

583 for 10 minutes at RT, then incubated overnight in 125 nM of Intercalator-Ir (Standard BioTools)

584 at 4°C. Cells were washed twice with cell staining buffer (Standard BioTools) and then

585 resuspended at a concentration of 1 million cells/ml in cell acquisition solution containing a 1:9

586 dilution of EQ 4 Element Beads (Standard BioTools). The samples were acquired on a Helios

587 (Standard BioTools) at an event rate of less than 500 events/s. After acquisition, ~~the~~ data were

588 normalized using bead-based normalization in the CyTOF software and gated to exclude residual

589 normalization beads, debris, dead cells, and doublets, leaving $DNA^+CD45^+Cisplatin^{lo}$ events for

590 subsequent clustering and high-dimensional analyses.

591

Virus titer by plaque assay

593 Virus or tissue homogenate supernatants were serially diluted in DMEM and titered on VeroE6

594 (for SARS-CoV-2), Vero81 (for MERS-CoV) or MDCK (for PR8) cells as previously described.

595

CyTOF data analysis

597 CyTOF data were analyzed using a combination of the Cytobank software package (77) and the

598 CyTOF workflow (78), which consists of a suite of packages (79) available in R (https://www.r-

599 project.org/). For analysis conducted within the CyTOF workflow, FlowJo Workspace files were

22

600 imported and parsed using functions within flowWorkspace and CytoML. An arcsinh
601 transformation (cofactor=5) was applied to the data using the dataPrep function within
602 CATALYST and stored as a "singlecellexperiment" object. Cell population clustering and
603 visualization were conducted using FlowSOM (80) and ConsensusClusterPlus (79) within the
604 CyTOF workflow and using the viSNE application within Cytobank. Clustering was performed
605 using data across all donors and time points. Additionally, clustering was performed either using
606 all live CD45$^+$ cells or after gating on CD66b$^+$ neutrophils.

607

608 *Analysis of human neutrophil proteomes*

609 NDNs and LDNs were isolated from whole blood by plasma Percoll gradients, followed by
610 magnetic bead purification, as previously described (81). For mass spectrometry, cells were
611 disrupted by sonication, followed by protein extraction with 2% sodium dodecyl sulfate. Protein
612 extracts were digested using an S-trap micro spin column (Protifi, LLC, Fairport, NY) digestion
613 protocol. For proteomic analyses, a Dionex Ultimate3000 RSLCnano system (ThermoFisher) was
614 used to inject the digests (250ng) onto a 300μm×5mm, 5μm PepMap^{TM} Neo C18 trap cartridge
615 heated at 30°C (ThermoFisher Scientific). The trapped peptides were then resolved using a
616 75μm×15cm, 3μm, 100Å PepMap^{TM} RSLC C18 EASY-spray separating column heated at 40°C
617 with a 90min 5-35% acetonitrile gradient accomplished at 200nl. An EASY-spray source
618 (ThermoFisher) was used to control ion transfer into the mass spectrometer at 320°C and 1.8kV.
619 An Orbitrap Exploris 480 mass spectrometer (ThermoFisher) was used to collect data from the LC
620 eluate. A Full MS-ddMS2 method with a 3sec cycle time was created in Xcalibur v4.5.445.18
621 (ThermoFisher) operating in positive polarity. Scan event one of the methods obtained an MS1
622 scan (60,000 resolution, Normalized AGC target of 100%, scan range 350-1400m/z). Scan event
623 two obtained dd-MS2 scans (7,500 resolution, Normalized AGC target of 50%) on ions with
624 charge states from 2-6 and a minimum intensity of 8,000 until the cycle time was complete.

625 Proteome Discoverer v2.5.0.400 (ThermoFisher) was used to analyze the data collected by the
626 mass spectrometer. In the processing step, the database used in SequestHT was the 7/17/2023
627 version of the UniprotKB reviewed canonical Homo sapiens sequences (Proteome ID
628 UP000005640). Trypsin (KR|P) digestion with up to two missed cleavages was assumed with the
629 dynamic modifications Oxidation (M), Acetyl (Protein N-term), Met-los (Protein N-term), and
630 Met-loss+Acetyl (Protein N-term); and the static modification Carbamidomethyl (C). Precursor,

631   and fragment mass tolerances were 10ppm and 0.02Da, respectively. In the consensus step,

632   proteins were quantified from the summed abundances of all high confidence unique and razor

633   peptide intensities. Samples were normalized to total peptide amount and scaled to 100%. Proteins

634   were grouped by the strict parsimony principle. Peptides and proteins were accepted at 1% FDR

635   for high confidence or 5% for medium confidence based on the q-value. A proteins text file was

636   exported from the consensus workflow result of Proteome Discoverer for curation in Microsoft

637   Excel.

638   Data from differentially expressed proteins were analyzed by MetaboAnalyst (V5.0). Partial

639   Least Squares Discrimination Analysis of differential protein expression among the cell groups

640   was created to establish differences among the groups. A correlation analysis of proteins

641   differentially expressed in the neutrophil populations was plotted. Analysis of differentially

642   expressed proteins was performed using Gene Ontology Enrichment Analysis. Protein-protein

643   interaction network analysis was performed using Search Tool for the Retrieval of Interacting

644   Genes/Proteins, STRING v10, with the highest confidence score (0.900).

645

646   *Statistics and reproducibility*

647   Differences between group means were analyzed by ANOVA (with Tukey's multiple

648   comparisons) and Student's t-tests, and differences in time-to-death were analyzed by log-rank

649   (Mantel-Cox) tests using Microsoft Excel and GraphPad Prism 8. All results are expressed as mean

650   ± standard error of the mean and were corrected for multiple comparisons. The association between

651   human peripheral blood LDNs and days post discharge, the association between mouse neutrophil

652   numbers and weight change (Figure. 1E, 3E, 3G, 4B, and 4C), and the association between mouse

653   neutrophil numbers and plasma CXCL12 (Figure. 5A, 7B and 7C) were analyzed by Simple Linear

654   Regression. The relationship between patient plasma CXCL12 and the frequency of LDNs (Figure.

655   2B and D) was analyzed via Repeated Measures Correlation. $P<0.05$ was considered statistically

656   significant. *$P<0.05$, **$P<0.01$, ***$P<0.001$, ****$P<0.0001$.

657

658   *Study approval*

659   Approval for using human samples was obtained from the IRB at the University of Louisville.

660   Written informed consent was obtained from either participants or their legal authorized

661   representatives (IRB 20. 0321). All animal studies were approved by the University of Iowa and

662 University of Louisville Animal Care and Use Committees and met stipulations of the Guide for

663 the Care and Use of Laboratory Animals.

664

665 *Data availability*

666 The data supporting the findings of this study are documented within the paper and are available

667 from the corresponding authors upon request. Correspondence and requests for materials should

668 be addressed to: Stanley Perlman (stanley-perlman@uiowa.edu) or Jian Zheng

669 (jian.zheng.1@louisville.edu).

670

References

671

672 1. Goyal P, Choi JJ, Pinheiro LC, Schenck EJ, Chen R, Jabri A, et al. Clinical Characteristics
673 of Covid-19 in New York City. *N Engl J Med.* 2020;382(24):2372-4.
674 2. Vabret N, Britton GJ, Gruber C, Hegde S, Kim J, Kuksin M, et al. Immunology of COVID-
675 19: Current State of the Science. *Immunity.* 2020;52(6):910-41.
676 3. Zhang W, Chua BY, Selva KJ, Kedzierski L, Ashhurst TM, Haycroft ER, et al. SARS-
677 CoV-2 infection results in immune responses in the respiratory tract and peripheral blood
678 that suggest mechanisms of disease severity. *Nat Commun.* 2022;13(1):2774.
679 4. Lowery SA, Sariol A, and Perlman S. Innate immune and inflammatory responses to
680 SARS-CoV-2: Implications for COVID-19. *Cell Host Microbe.* 2021.
681 5. Cavalli G, Larcher A, Tomelleri A, Campochiaro C, Della-Torre E, De Luca G, et al.
682 Interleukin-1 and interleukin-6 inhibition compared with standard management in patients
683 with COVID-19 and hyperinflammation: a cohort study. *Lancet Rheumatol.*
684 2021;3(4):e253-e61.
685 6. Carissimo G, Xu W, Kwok I, Abdad MY, Chan YH, Fong SW, et al. Whole blood
686 immunophenotyping uncovers immature neutrophil-to-VD2 T-cell ratio as an early marker
687 for severe COVID-19. *Nat Commun.* 2020;11(1):5243.
688 7. Mirchandani AS, Jenkins SJ, Bain CC, Sanchez-Garcia MA, Lawson H, Coelho P, et al.
689 Hypoxia shapes the immune landscape in lung injury and promotes the persistence of
690 inflammation. *Nat Immunol.* 2022;23(6):927-39.
691 8. Cao X. COVID-19: immunopathology and its implications for therapy. *Nat Rev Immunol.*
692 2020;20(5):269-70.
693 9. Morrissey SM, Geller AE, Hu X, Tieri D, Ding C, Klaes CK, et al. A specific low-density
694 neutrophil population correlates with hypercoagulation and disease severity in hospitalized
695 COVID-19 patients. *JCI Insight.* 2021;6(9).
696 10. Hacbarth E, and Kajdacsy-Balla A. Low density neutrophils in patients with systemic lupus
697 erythematosus, rheumatoid arthritis, and acute rheumatic fever. *Arthritis Rheum.*
698 1986;29(11):1334-42.
699 11. Cilenti F, Barbiera G, Caronni N, Iodice D, Montaldo E, Barresi S, et al. A PGE2-MEF2A
700 axis enables context-dependent control of inflammatory gene expression. *Immunity.*
701 2021;54(8):1665-82 e14.
702 12. Carmona-Rivera C, and Kaplan MJ. Low-density granulocytes in systemic autoimmunity
703 and autoinflammation. *Immunol Rev.* 2023;314(1):313-25.
704 13. Dinnon KH, 3rd, Leist SR, Schafer A, Edwards CE, Martinez DR, Montgomery SA, et al.
705 A mouse-adapted model of SARS-CoV-2 to test COVID-19 countermeasures. *Nature.*
706 2020;586(7830):560-6.
707 14. Montaldo E, Lusito E, Bianchessi V, Caronni N, Scala S, Basso-Ricci L, et al. Cellular and
708 transcriptional dynamics of human neutrophils at steady state and upon stress. *Nat
709 Immunol.* 2022;23(10):1470-83.
710 15. McLeish KR, Shrestha R, Vashishta A, Rane MJ, Barati MT, Brier ME, et al. Differential
711 Functional Responses of Neutrophil Subsets in Severe COVID-19 Patients. *Front
712 Immunol.* 2022;13:879686.
713 16. Weeratunga P, Denney L, Bull JA, Repapi E, Sergeant M, Etherington R, et al. Single cell
714 spatial analysis reveals inflammatory foci of immature neutrophil and CD8 T cells in
715 COVID-19 lungs. *Nat Commun.* 2023;14(1):7216.

716 17. Guo Q, Zhao Y, Li J, Liu J, Yang X, Guo X, et al. Induction of alarmin S100A8/A9
717   mediates activation of aberrant neutrophils in the pathogenesis of COVID-19. *Cell Host*
718   *Microbe.* 2021;29(2):222-35 e4.
719 18. Schulte-Schrepping J, Reusch N, Paclik D, Bassler K, Schlickeiser S, Zhang B, et al.
720   Severe COVID-19 Is Marked by a Dysregulated Myeloid Cell Compartment. *Cell.*
721   2020;182(6):1419-40 e23.
722 19. Silvin A, Chapuis N, Dunsmore G, Goubet AG, Dubuisson A, Derosa L, et al. Elevated
723   Calprotectin and Abnormal Myeloid Cell Subsets Discriminate Severe from Mild COVID-
724   19. *Cell.* 2020;182(6):1401-18 e18.
725 20. Wilk AJ, Rustagi A, Zhao NQ, Roque J, Martinez-Colon GJ, McKechnie JL, et al. A
726   single-cell atlas of the peripheral immune response in patients with severe COVID-19. *Nat*
727   *Med.* 2020;26(7):1070-6.
728 21. Cabrera LE, Pekkarinen PT, Alander M, Nowlan KHA, Nguyen NA, Jokiranta S, et al.
729   Characterization of low-density granulocytes in COVID-19. *PLoS Pathog.*
730   2021;17(7):e1009721.
731 22. Chittimalli K, Jahan J, Sakamuri A, Weyrick H, Winkle W, Adkins S, et al. Reversal of
732   aging-associated increase in myelopoiesis and expression of alarmins by angiotensin-(1-
733   7). *Sci Rep.* 2023;13(1):2543.
734 23. Park MD, Le Berichel J, Hamon P, Wilk CM, Belabed M, Yatim N, et al. Hematopoietic
735   aging promotes cancer by fueling IL-1α-driven emergency myelopoiesis. *Science.*
736   2024;386(6720):eadn0327.
737 24. Nacionales DC, Szpila B, Ungaro R, Lopez MC, Zhang J, Gentile LF, et al. A Detailed
738   Characterization of the Dysfunctional Immunity and Abnormal Myelopoiesis Induced by
739   Severe Shock and Trauma in the Aged. *J Immunol.* 2015;195(5):2396-407.
740 25. George PM, Reed A, Desai SR, Devaraj A, Faiez TS, Laverty S, et al. A persistent
741   neutrophil-associated immune signature characterizes post-COVID-19 pulmonary
742   sequelae. *Sci Transl Med.* 2022;14(671):eabo5795.
743 26. Nathan C. Neutrophils and COVID-19: Nots, NETs, and knots. *J Exp Med.* 2020;217(9).
744 27. Agrati C, Sacchi A, Bordoni V, Cimini E, Notari S, Grassi G, et al. Expansion of myeloid-
745   derived suppressor cells in patients with severe coronavirus disease (COVID-19). *Cell*
746   *Death Differ.* 2020;27(11):3196-207.
747 28. Vijayakumar B, Boustani K, Ogger PP, Papadaki A, Tonkin J, Orton CM, et al. Immuno-
748   proteomic profiling reveals aberrant immune cell regulation in the airways of individuals
749   with ongoing post-COVID-19 respiratory disease. *Immunity.* 2022;55(3):542-56 e5.
750 29. Nauseef WM. Human neutrophils not equal murine neutrophils: Does it matter? *Immunol*
751   *Rev.* 2022.
752 30. Boudewijns R, Thibaut HJ, Kaptein SJF, Li R, Vergote V, Seldeslachts L, et al. STAT2
753   signaling restricts viral dissemination but drives severe pneumonia in SARS-CoV-2
754   infected hamsters. *Nat Commun.* 2020;11(1):5838.
755 31. Fahlberg MD, Blair RV, Doyle-Meyers LA, Midkiff CC, Zenere G, Russell-Lodrigue KE,
756   et al. Cellular events of acute, resolving or progressive COVID-19 in SARS-CoV-2
757   infected non-human primates. *Nat Commun.* 2020;11(1):6078.
758 32. Wong LR, Zheng J, Wilhelmsen K, Li K, Ortiz ME, Schnicker NJ, et al. Eicosanoid
759   signalling blockade protects middle-aged mice from severe COVID-19. *Nature.*
760   2022;605(7908):146-51.

761 33. Zheng J, Wong LR, Li K, Verma AK, Ortiz ME, Wohlford-Lenane C, et al. COVID-19
762   treatments and pathogenesis including anosmia in K18-hACE2 mice. *Nature.*
763   2021;589(7843):603-7.
764 34. Munoz-Fontela C, Widerspick L, Albrecht RA, Beer M, Carroll MW, de Wit E, et al.
765   Advances and gaps in SARS-CoV-2 infection models. *PLoS Pathog.*
766   2022;18(1):e1010161.
767 35. Gu H, Chen Q, Yang G, He L, Fan H, Deng YQ, et al. Adaptation of SARS-CoV-2 in
768   BALB/c mice for testing vaccine efficacy. *Science.* 2020;369(6511):1603-7.
769 36. Chua RL, Lukassen S, Trump S, Hennig BP, Wendisch D, Pott F, et al. COVID-19 severity
770   correlates with airway epithelium-immune cell interactions identified by single-cell
771   analysis. *Nat Biotechnol.* 2020;38(8):970-9.
772 37. Furze RC, and Rankin SM. Neutrophil mobilization and clearance in the bone marrow.
773   *Immunology.* 2008;125(3):281-8.
774 38. Nauseef WM, and Borregaard N. Neutrophils at work. *Nat Immunol.* 2014;15(7):602-11.
775 39. Furze RC, and Rankin SM. The role of the bone marrow in neutrophil clearance under
776   homeostatic conditions in the mouse. *FASEB J.* 2008;22(9):3111-9.
777 40. Dwivedi A, Ui Mhaonaigh A, Carroll M, Khosravi B, Batten I, Ballantine RS, et al.
778   Emergence of dysfunctional neutrophils with a defect in arginase-1 release in severe
779   COVID-19. *JCI Insight.* 2024;9(17).
780 41. Evrard M, Kwok IWH, Chong SZ, Teng KWW, Becht E, Chen J, et al. Developmental
781   Analysis of Bone Marrow Neutrophils Reveals Populations Specialized in Expansion,
782   Trafficking, and Effector Functions. *Immunity.* 2018;48(2):364-79 e8.
783 42. Janssens R, Struyf S, and Proost P. Pathological roles of the homeostatic chemokine
784   CXCL12. *Cytokine Growth Factor Rev.* 2018;44:51-68.
785 43. Shebl FM, Pinto LA, Garcia-Pineres A, Lempicki R, Williams M, Harro C, et al.
786   Comparison of mRNA and protein measures of cytokines following vaccination with
787   human papillomavirus-16 L1 virus-like particles. *Cancer Epidemiol Biomarkers Prev.*
788   2010;19(4):978-81.
789 44. Anderson L, and Seilhamer J. A comparison of selected mRNA and protein abundances in
790   human liver. *Electrophoresis.* 1997;18(3-4):533-7.
791 45. Koussounadis A, Langdon SP, Um IH, Harrison DJ, and Smith VA. Relationship between
792   differentially expressed mRNA and mRNA-protein correlations in a xenograft model
793   system. *Sci Rep.* 2015;5:10775.
794 46. Misra P, Lebeche D, Ly H, Schwarzkopf M, Diaz G, Hajjar RJ, et al. Quantitation of
795   CXCR4 expression in myocardial infarction using 99mTc-labeled SDF-1alpha. *J Nucl*
796   *Med.* 2008;49(6):963-9.
797 47. Zhao F, Lu Y, Li Z, He J, Cui N, Luo L, et al. The CXCR4-CXCL12 axis promotes T cell
798   reconstitution via efficient hematopoietic immigration. *J Genet Genomics.* 2022.
799 48. Xu SW, Ilyas I, and Weng JP. Endothelial dysfunction in COVID-19: an overview of
800   evidence, biomarkers, mechanisms and potential therapies. *Acta Pharmacol Sin.*
801   2023;44(4):695-709.
802 49. Chong Z, Karl CE, Halfmann PJ, Kawaoka Y, Winkler ES, Keeler SP, et al. Nasally
803   delivered interferon-lambda protects mice against infection by SARS-CoV-2 variants
804   including Omicron. *Cell Rep.* 2022;39(6):110799.

805   50.   Xu ZS, Shu T, Kang L, Wu D, Zhou X, Liao BW, et al. Temporal profiling of plasma
806   cytokines, chemokines and growth factors from mild, severe and fatal COVID-19 patients.
807   *Signal Transduct Target Ther.* 2020;5(1):100.

808   51.   Martinez-Fleta P, Vera-Tome P, Jimenez-Fernandez M, Requena S, Roy-Vallejo E, Sanz-
809   Garcia A, et al. A Differential Signature of Circulating miRNAs and Cytokines Between
810   COVID-19 and Community-Acquired Pneumonia Uncovers Novel Physiopathological
811   Mechanisms of COVID-19. *Front Immunol.* 2021;12:815651.

812   52.   Korayem OH, Ahmed AE, Meabed MH, Magdy DM, and Abdelghany WM. Genetic clues
813   to COVID-19 severity: exploring the stromal cell-derived factor-1/CXCL12 rs2839693
814   polymorphism in adult Egyptians. *BMC Infect Dis.* 2023;23(1):702.

815   53.   Thwaites RS, Sanchez Sevilla Uruchurtu A, Siggins MK, Liew F, Russell CD, Moore SC,
816   et al. Inflammatory profiles across the spectrum of disease reveal a distinct role for GM-
817   CSF in severe COVID-19. *Sci Immunol.* 2021;6(57).

818   54.   Muus C, Luecken MD, Eraslan G, Sikkema L, Waghray A, Heimberg G, et al. Single-cell
819   meta-analysis of SARS-CoV-2 entry genes across tissues and demographics. *Nat Med.*
820   2021;27(3):546-59.

821   55.   Pelle MC, Zaffina I, Luca S, Forte V, Trapanese V, Melina M, et al. Endothelial
822   Dysfunction in COVID-19: Potential Mechanisms and Possible Therapeutic Options. *Life*
823   *(Basel).* 2022;12(10).

824   56.   Zhou Q, Zhang L, Dong Y, Wang Y, Zhang B, Zhou S, et al. The role of SARS-CoV-2-
825   mediated NF-kappaB activation in COVID-19 patients. *Hypertens Res.* 2024;47(2):375-
826   84.

827   57.   Eash KJ, Greenbaum AM, Gopalan PK, and Link DC. CXCR2 and CXCR4
828   antagonistically regulate neutrophil trafficking from murine bone marrow. *J Clin Invest.*
829   2010;120(7):2423-31.

830   58.   Chandrasekaran P, Negretti NM, Sivakumar A, Liberti DC, Wen H, Peers de Nieuwburgh
831   M, et al. CXCL12 defines lung endothelial heterogeneity and promotes distal vascular
832   growth. *Development.* 2022;149(21).

833   59.   Brandes M, Klauschen F, Kuchen S, and Germain RN. A systems analysis identifies a
834   feedforward inflammatory circuit leading to lethal influenza infection. *Cell.*
835   2013;154(1):197-212.

836   60.   Speaks S, McFadden MI, Zani A, Solstad A, Leumi S, Roettger JE, et al. Gasdermin D
837   promotes influenza virus-induced mortality through neutrophil amplification of
838   inflammation. *Nat Commun.* 2024;15(1):2751.

839   61.   Dinnon KH, 3rd, Leist SR, Okuda K, Dang H, Fritch EJ, Gully KL, et al. SARS-CoV-2
840   infection produces chronic pulmonary epithelial and immune cell dysfunction with fibrosis
841   in mice. *Sci Transl Med.* 2022:eabo5070.

842   62.   Frere JJ, Serafini RA, Pryce KD, Zazhytska M, Oishi K, Golynker I, et al. SARS-CoV-2
843   infection in hamsters and humans results in lasting and unique systemic perturbations after
844   recovery. *Sci Transl Med.* 2022;14(664):eabq3059.

845   63.   Verma AK, Zheng J, Meyerholz DK, and Perlman S. SARS-CoV-2 infection of
846   sustentacular cells disrupts olfactory signaling pathways. *JCI Insight.* 2022;7(24).

847   64.   Sieminska I, Weglarczyk K, Surmiak M, Kurowska-Baran D, Sanak M, Siedlar M, et al.
848   Mild and Asymptomatic COVID-19 Convalescents Present Long-Term Endotype of
849   Immunosuppression Associated With Neutrophil Subsets Possessing Regulatory
850   Functions. *Front Immunol.* 2021;12:748097.

851 65. Jamieson KC, Traves SL, Kooi C, Wiehler S, Dumonceaux CJ, Maciejewski BA, et al.
852 Rhinovirus and Bacteria Synergistically Induce IL-17C Release from Human Airway
853 Epithelial Cells To Promote Neutrophil Recruitment. *J Immunol.* 2019;202(1):160-70.

854 66. Sun R, Huang J, Yang Y, Liu L, Shao Y, Li L, et al. Dysfunction of low-density neutrophils
855 in peripheral circulation in patients with sepsis. *Sci Rep.* 2022;12(1):685.

856 67. Nagasawa T, Hirota S, Tachibana K, Takakura N, Nishikawa S, Kitamura Y, et al. Defects
857 of B-cell lymphopoiesis and bone-marrow myelopoiesis in mice lacking the CXC
858 chemokine PBSF/SDF-1. *Nature.* 1996;382(6592):635-8.

859 68. Ma Q, Jones D, Borghesani PR, Segal RA, Nagasawa T, Kishimoto T, et al. Impaired B-
860 lymphopoiesis, myelopoiesis, and derailed cerebellar neuron migration in CXCR4- and
861 SDF-1-deficient mice. *Proc Natl Acad Sci U S A.* 1998;95(16):9448-53.

862 69. Kohli K, Pillarisetty VG, and Kim TS. Key chemokines direct migration of immune cells
863 in solid tumors. *Cancer Gene Ther.* 2022;29(1):10-21.

864 70. Fearon DT. The carcinoma-associated fibroblast expressing fibroblast activation protein
865 and escape from immune surveillance. *Cancer Immunol Res.* 2014;2(3):187-93.

866 71. McCandless EE, Zhang B, Diamond MS, and Klein RS. CXCR4 antagonism increases T
867 cell trafficking in the central nervous system and improves survival from West Nile virus
868 encephalitis. *Proc Natl Acad Sci U S A.* 2008;105(32):11270-5.

869 72. McCandless EE, Wang Q, Woerner BM, Harper JM, and Klein RS. CXCL12 limits
870 inflammation by localizing mononuclear infiltrates to the perivascular space during
871 experimental autoimmune encephalomyelitis. *J Immunol.* 2006;177(11):8053-64.

872 73. Carbajal KS, Schaumburg C, Strieter R, Kane J, and Lane TE. Migration of engrafted
873 neural stem cells is mediated by CXCL12 signaling through CXCR4 in a viral model of
874 multiple sclerosis. *Proc Natl Acad Sci U S A.* 2010;107(24):11068-73.

875 74. Li K, Wohlford-Lenane CL, Channappanavar R, Park JE, Earnest JT, Bair TB, et al.
876 Mouse-adapted MERS coronavirus causes lethal lung disease in human DPP4 knockin
877 mice. *Proc Natl Acad Sci U S A.* 2017;114(15):E3119-E28.

878 75. Qing E, Kicmal T, Kumar B, Hawkins GM, Timm E, Perlman S, et al. Dynamics of SARS-
879 CoV-2 Spike Proteins in Cell Entry: Control Elements in the Amino-Terminal Domains.
880 *mBio.* 2021;12(4):e0159021.

881 76. Meyerholz DK, and Beck AP. Principles and approaches for reproducible scoring of tissue
882 stains in research. *Lab Invest.* 2018;98(7):844-55.

883 77. Chen TJ, and Kotecha N. Cytobank: providing an analytics platform for community
884 cytometry data analysis and collaboration. *Curr Top Microbiol Immunol.* 2014;377:127-
885 57.

886 78. Nowicka M, Krieg C, Crowell HL, Weber LM, Hartmann FJ, Guglietta S, et al. CyTOF
887 workflow: differential discovery in high-throughput high-dimensional cytometry datasets.
888 *F1000Res.* 2017;6:748.

889 79. Wilkerson MD, and Hayes DN. ConsensusClusterPlus: a class discovery tool with
890 confidence assessments and item tracking. *Bioinformatics.* 2010;26(12):1572-3.

891 80. Van Gassen S, Callebaut B, Van Helden MJ, Lambrecht BN, Demeester P, Dhaene T, et
892 al. FlowSOM: Using self-organizing maps for visualization and interpretation of cytometry
893 data. *Cytometry A.* 2015;87(7):636-45.

894 81. McLeish KR, Merchant ML, Creed TM, Tandon S, Barati MT, Uriarte SM, et al. Frontline
895 Science: Tumor necrosis factor-alpha stimulation and priming of human neutrophil granule
896 exocytosis. *J Leukoc Biol.* 2017;102(1):19-29.

Author contributions

J.Z. designed the study and experiments, collected data, and contributed to data interpretation and manuscript preparation. H.D., E.Q., R.S., A.E.G., S.M.M., D.S., X.H., H.L., H.L., and D.M. contributed to data collection and interpretation. K.W. and K.K. contributed to study design. L.H.W. and P.T.E. contributed to data statistical analysis and interpretation. P.S.H., W.J.J., and R.B. contributed to obtaining permission to biobank lung samples from patients, storing samples, analyzing the histopathology, and providing clinical data on the patients. D.K.M. contributed to Histopathology and scoring. K.P. and S.M.U. contributed to data interpretation and manuscript preparation. M.L.M. contributed to data generation and data analysis in the proteomic analysis. K.M., T.G., J.H. and J.Y. designed experiments and contributed to data interpretation and manuscript preparation. S.P. designed and coordinated the study, designed experiments and contributed to data interpretation, data presentation and manuscript preparation.

31

Figures

917
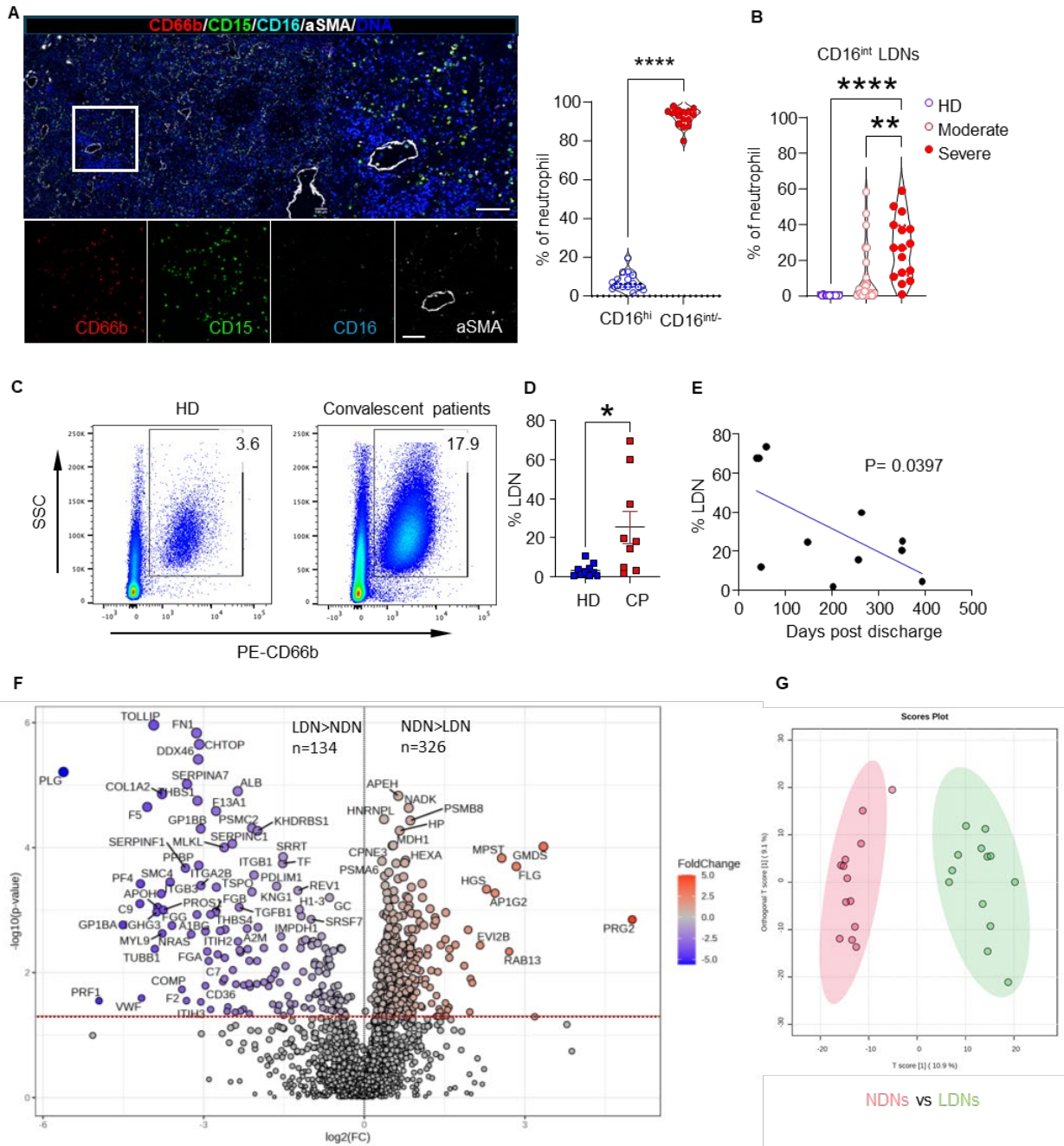
Figure 1: Neutrophilia and accumulated LDNs in COVID-19 patients. (**A**) Massive infiltration
of LDNs in the lungs of deceased COVID-19 patients was identified with metal isotope-labeled
antibodies (left and right panels). Images are representative of 5 slides from 5 deceased COVID-
19 cases. Scale bar=100μm. The percentage of CD16^{hi} and CD16^{int} neutrophils in 3 regions of
interest (ROIs) of each slide (middle panel) was quantitated by Flowjo after converting imaging
files into .fcs file. ****P-values< 0.0001 by t-test. (**B**) Peripheral blood LDNs in healthy donors

924   (HD, n=13) and COVID-19 patients with moderate (n=23) or severe disease (n=16). **P-values<

925   0.01, ****P-values< 0.0001 by ANOVA. (**C-E**) A cohort of convalescent COVID-19 patients and

926   healthy donors were recruited at times ranging from 1 month to 13 months after hospital discharge.

927   A representative flow plot (**C**) and summary (**D**) of CD66b$^+$ LDN frequency in the peripheral

928   blood of convalescent patients (CP, collected at 1-13 months post discharge) and age-matched

929   healthy donors (HD) are shown. n=11. *P-values< 0.05 by t-test. (**E**) Frequency of LDNs was

930   negatively correlated with time from discharge (each point represents the data obtained from an

931   individual patient). (**F** and **G**) A total of 1830 proteins were identified by mass spectrometry of

932   normal-density neutrophils (NDNs) and low-density neutrophils (LDNs) analyzed from each of

933   13 patients with severe COVID-19. Proteins were quantified from average peptide expression of

934   pooled data using Scaffold, and differential expression of proteins (DEP) was determined by

935   analysis with MetaboAnalyst. (**F**) A volcano plot of the 1830 proteins expressed by NDNs and

936   LDNs from COVID-19 patients, comparing log2 of fold change to -log10(p value), with proteins

937   above the red line possessing a p value<0.05. 326 proteins show significantly greater expression

938   in NDNs, and 134 proteins show significantly greater expression in NDNs. (**G**) Differences in the

939   pattern of protein expression by LDNs and NDNs were compared using Orthogonal Partial Least

940   Squares Discriminant Analysis (orthoPLS-DA).
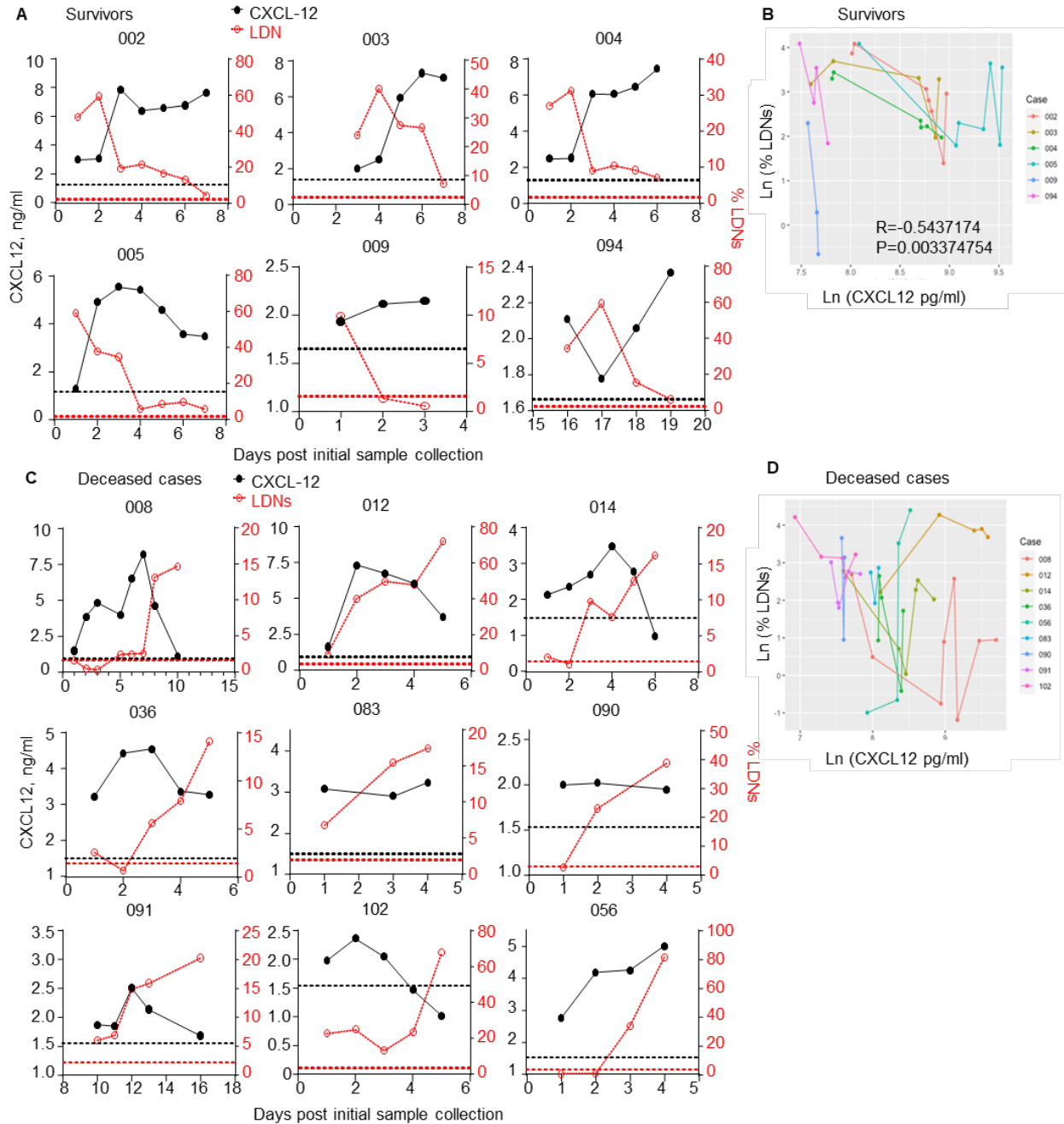
Figure 2: Plasma CXCL12 levels negatively correlate with peripheral blood LDNs in longitudinal analyses. (**A**) Peripheral blood samples from 6 SARS-CoV-2-infected survivors were collected longitudinally during hospitalization as described previously (9). Concentration of plasma CXCL12 and peripheral blood LDNs were measured. Black dotted line: average plasma CXCL12 of healthy donors. Red dot line: average LDNs of healthy donors. (**B**) Correlation between concentration of plasma CXCL12 and percentage of peripheral blood LDNs analyzed by Repeated Measures Correlation (with log transformation to Ln to meet linear assumption). R-

949   values=-0.5437174 (P=0.003374754). (**C**) Peripheral blood samples from 9 SARS-CoV-2-

950   infected deceased patients were collected at multiple time points during hospitalization as

951   described previously. Concentrations of plasma CXCL12 and peripheral blood LDNs are shown.

952   Black dot line: average CXCL12 of healthy donors. Red dot line: average LDNs of healthy donors.

953   (**D**) Correlation between concentration of plasma CXCL12 and percentage of peripheral blood

954   LDNs analyzed by Repeated Measures Correlation (with log transformation to Ln to meet linear

955   assumption). R-values=-0.01767992 (P=0. 9184839).

956
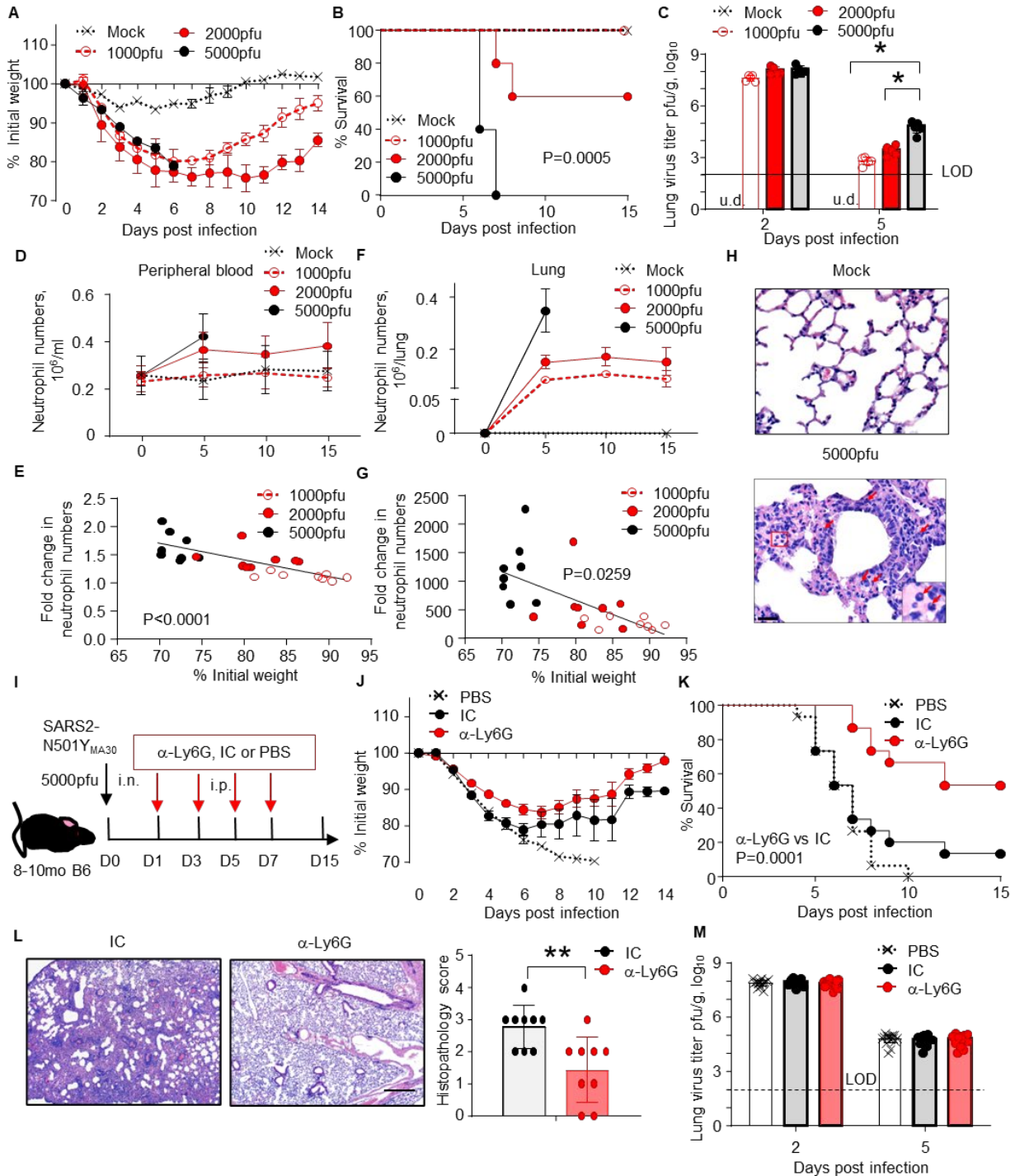
**Figure 3: Neutrophil depletion ameliorates disease severity of SARS2-N501Y$_{MA30}$- infected**

mice. 8-10-month-old (n=5, **A-C**) C57BL/6N mice were infected with 1000, 2000 or 5000 pfu

SARS2-N501Y$_{MA30}$. Weight (**A**), survival (**B**) and lung infectious virus titers (**C**) are shown. Data

are representative of three independent experiments. Data in **A** and **C** are mean±SEM. LOD, limit

of detection. u.d., undetected. ANOVA F-test P<0.05 in (**C**). (**D-H**) Middle-aged C57BL/6N mice

36

962 (8-10-month-old, n=5) were infected with 1000, 2000 or 5000 pfu SARS2-N501Y$_{MA30}$ virus. (**D**

963 and **F**) The number of neutrophils in peripheral blood (**D**) and lung (**F**) of infected (n=8) and

964 control mice (n=5) was determined by flow cytometry at the indicated time points. Data are

965 mean±SEM and are representative of three independent experiments. (**E** and **G**) The correlation

966 between the fold increase of peripheral blood (**E**) or lung-derived (**G**) neutrophils and weight

967 change of SARS2-N501Y$_{MA30}$-infected mice (n=8) at day 5 post infection is shown. Data are

968 representative of three independent experiments. (**H**) Infiltration of neutrophils (arrows) in lungs

969 of mock- or SARS2-N501Y$_{MA30}$-infected (5000pfu) mice. Images are representative of 3

970 independent experiments. Bar=25µm, arrows: PMNs. (**I-M**) 8–10-month-old C57BL/6N mice

971 were infected with 5000 pfu SARS2-N501Y$_{MA30}$ and treated with PBS, anti-Ly6G antibody or

972 isotype control (IC, isotype Ig) (n=15 mice/group). Weight (**J**), survival (**K**), lung histopathology

973 (**L**, bar = 430µm) and infectious virus titers (**M**) are shown. Data in **J** and **M** are mean±SEM.

974 LOD, limit of detection. Data in (**K**) are summary of three independent experiments. Data in (**L**)

975 are representative images and summary of two independent experiments (data are mean±SEM)

976 (n=9).
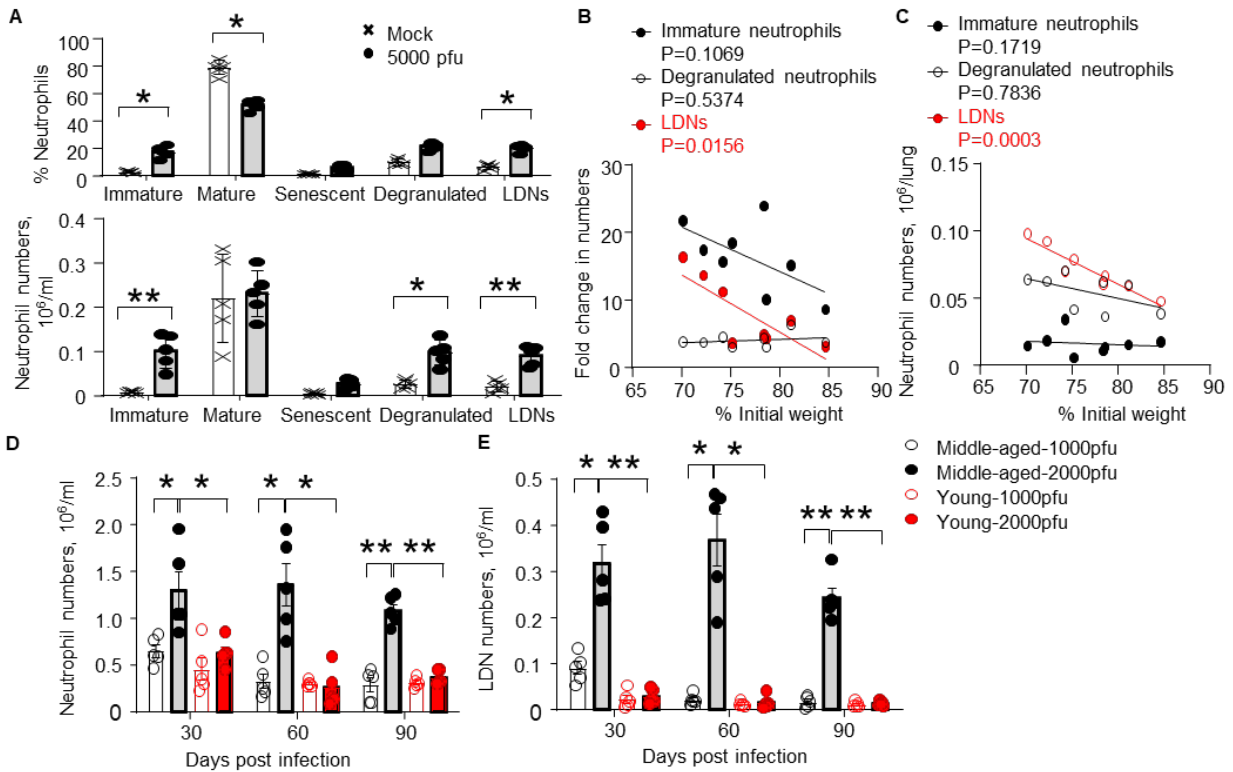
Figure 4: Accumulation of LDNs correlates with disease severity of SARS2-N501Y$_{MA30}$-infected mice. (**A**) The percentage and absolute number of peripheral blood neutrophil subsets (CD15$^+$CD16$^+$CD115$^-$CXCR2$^-$ (immature), CD16^{hi}CD62L^{hi}CXCR2^{hi}CXCR4^{low} (mature), CD11b^{hi} CXCR2^{low}CD62L^{low} CXCR4^{hi} (senescent), CD11b$^+$CD18$^+$Gr-1^{int} (degranulated), and ARG1$^+$CD15$^+$ CD33$^+$CD101$^-$CXCR4$^+$ (LDNs)) in SARS2-N501Y$_{MA30}$-infected mice at day 5 post infection (n=5). Data are mean±SEM and are representative of three independent experiments. *P-values<0.05, **P-values< 0.01 by t-test. (**B** and **C**) Correlation between fold increase of peripheral blood (**B**) and lung (**C**) immature neutrophils, degranulated neutrophils and LDNs, and weight change of SARS2-N501Y$_{MA30}$-infected mice at day 5 post infection (n=8). Peripheral blood: R-values=0.3744 (P=0.1069), 0.06653 (P=0.5374), and 0.6501 (P=0.0156) for immature neutrophils, degranulated neutrophils and LDNs. Lung: R-values=0.2862 (P=0.1719), 0.01357 (P=0.7836), and 0.9016 (P=0.0003) for immature neutrophils, degranulated neutrophils and LDNs,. Data are representative of two independent experiments. (**D** and **E**) Young (8-10-week-old) or middle-aged (8-10-month-old) C57BL/6N mice were sublethally infected with 1000 or 2000 pfu. The numbers of peripheral blood neutrophils (**D**) and LDNs (**E**) were determined at the indicated time points by

38

993   flow cytometry. n=5. Data are mean±SEM and are representative of two independent experiments.

994   *P-values< 0.05, ** P-values< 0.01 by ANOVA F-test.

995
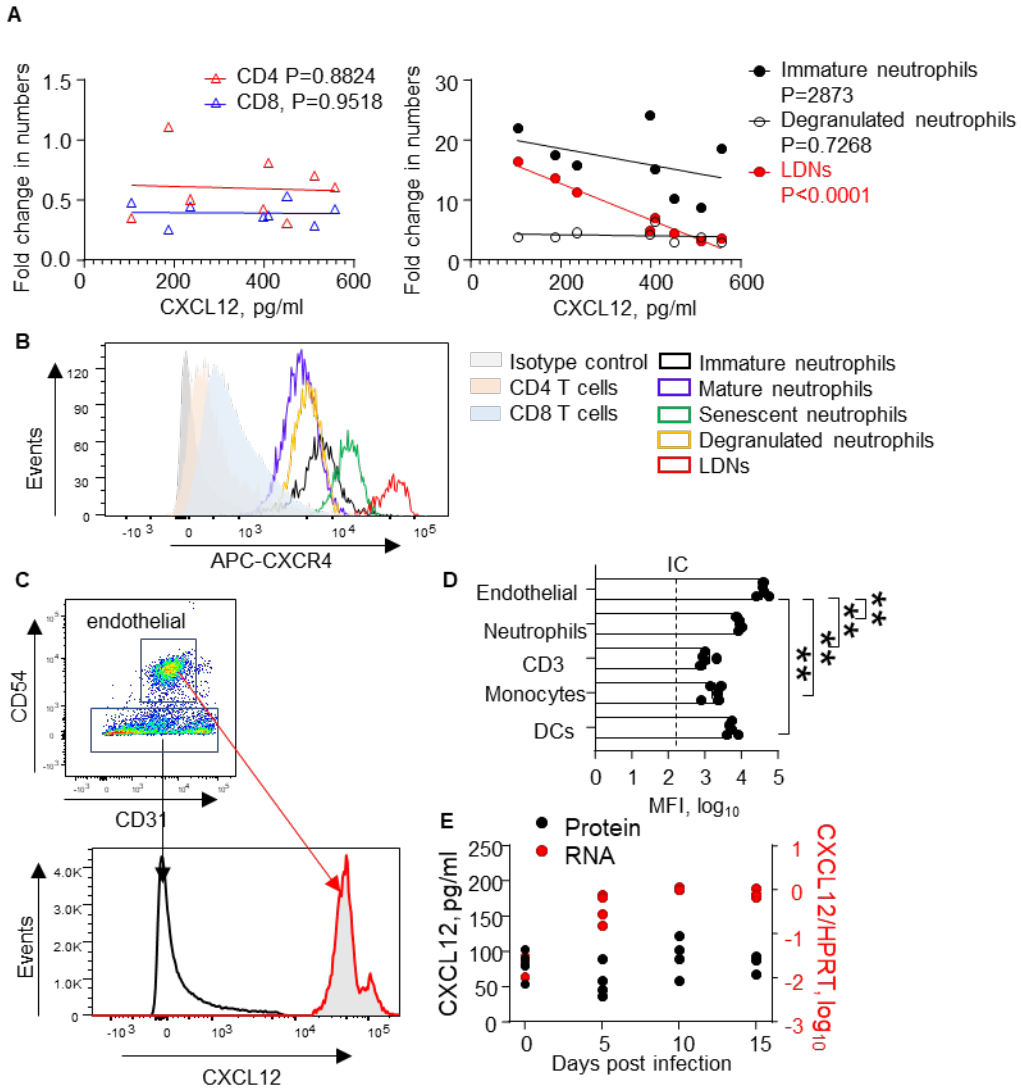
Figure 5: CXCL12-CXCR4 axis regulates blood neutrophil numbers in SARS2-N501Y$_{MA30}$-infected mice. (**A**) The correlation between the concentration of plasma CXCL12 and the fold change of peripheral blood CD4 and CD8 T cells, immature neutrophils, degranulated neutrophils, and LDNs in SARS2-N501Y$_{MA30}$-infected mice (5000 pfu) at day 5 post infection (n=8). R-values=0.003954 (P=0.8824) (CD4 T cells), 0.0006628 (P=0.9518) (CD8 T cells), 0.1851 (P=0.2873) (immature neutrophils) 0.02186 (P=0.7268) (degranulated neutrophils) and 0.9547 (P<0.0001) LDNs. Data are representative of three independent experiments. (**B**) Expression of CXCR4 by peripheral blood CD4 and CD8 T cells, and neutrophil subsets of mice infected with SARS2-N501Y$_{MA30}$ at day 5 post infection. (**C**) Expression of intracellular CXCL12 in CD45$^-$CD31$^+$CD54$^+$ vascular endothelial cells at day 5 post infection. (**D**) Summary of CXCL12 expression (MFI, mean fluorescence intensity) in peripheral blood cell subsets and endothelial

40

1007   cells, n=5. Data are representative of two independent experiments and are mean±SEM. **P-

1008   values<0.01 by ANOVA. (**E**) RNA (right y-axis) and protein (left y-axis) CXCL12 levels in

1009   homogenates of bone marrow harvested from SARS2-N501Y$_{MA30}$-infected mice were determined

1010   at the indicated time points by RT-qPCR and ELISA, respectively. n=4. Data are representative of

1011   two independent experiments.
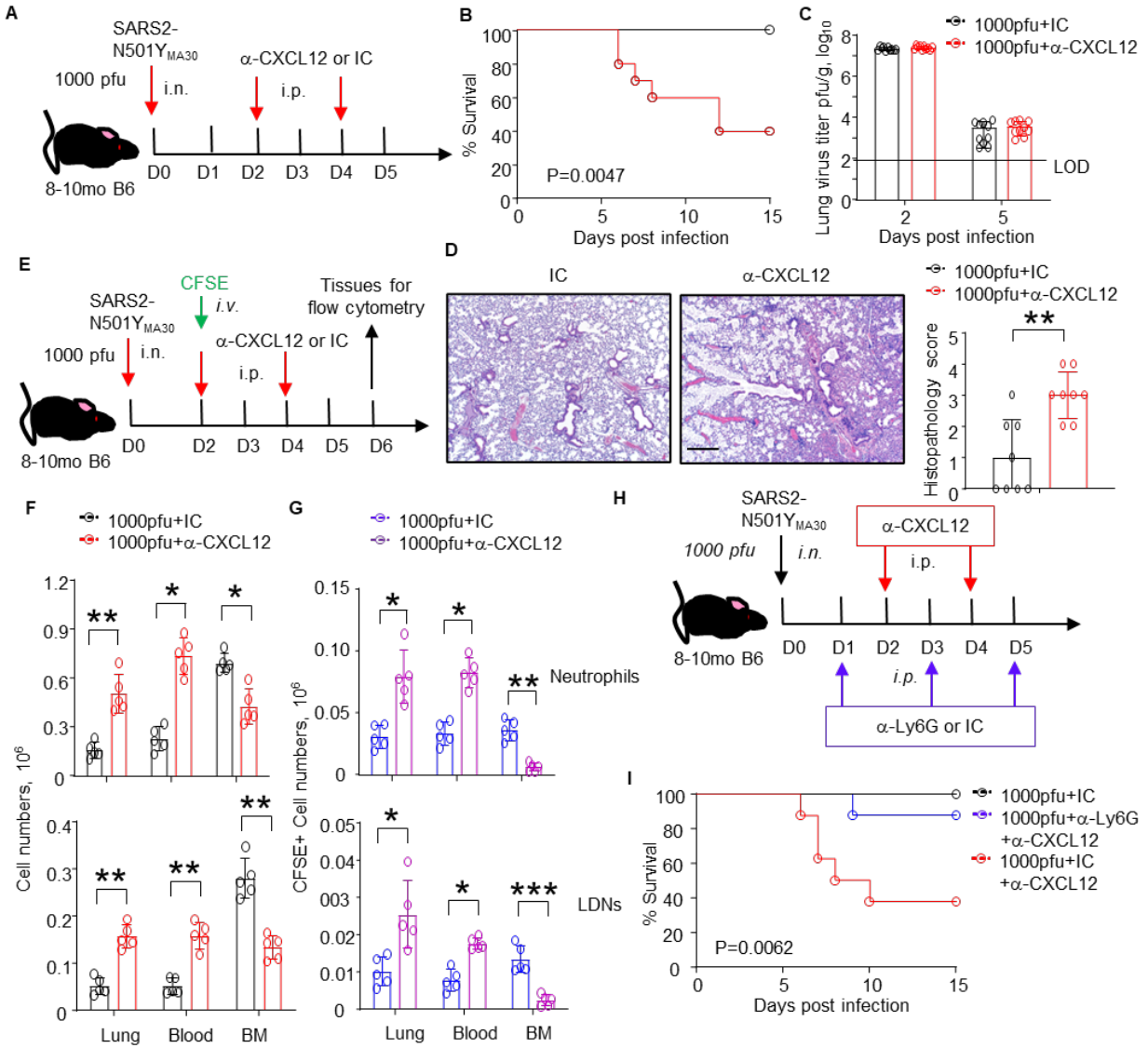
Figure 6: Blockade of CXCL12 modifies disease severity and neutrophil distribution. (**A-D**) Survival (**B**), lung histopathology (**C**, bar = 430μm), and infectious viral titers (**D**) of 8-10-month-old C57BL/6N mice infected with 1000 pfu SARS2-N501Y$_{MA30}$ followed by treatment of anti-CXCL12 antibody or its isotype control (IC, isotype Ig) (**A**). Data in (**B**) are summary of four independent experiments (n=20). Data in (**C**) are representative images and summary of two independent experiments (n=10, sampl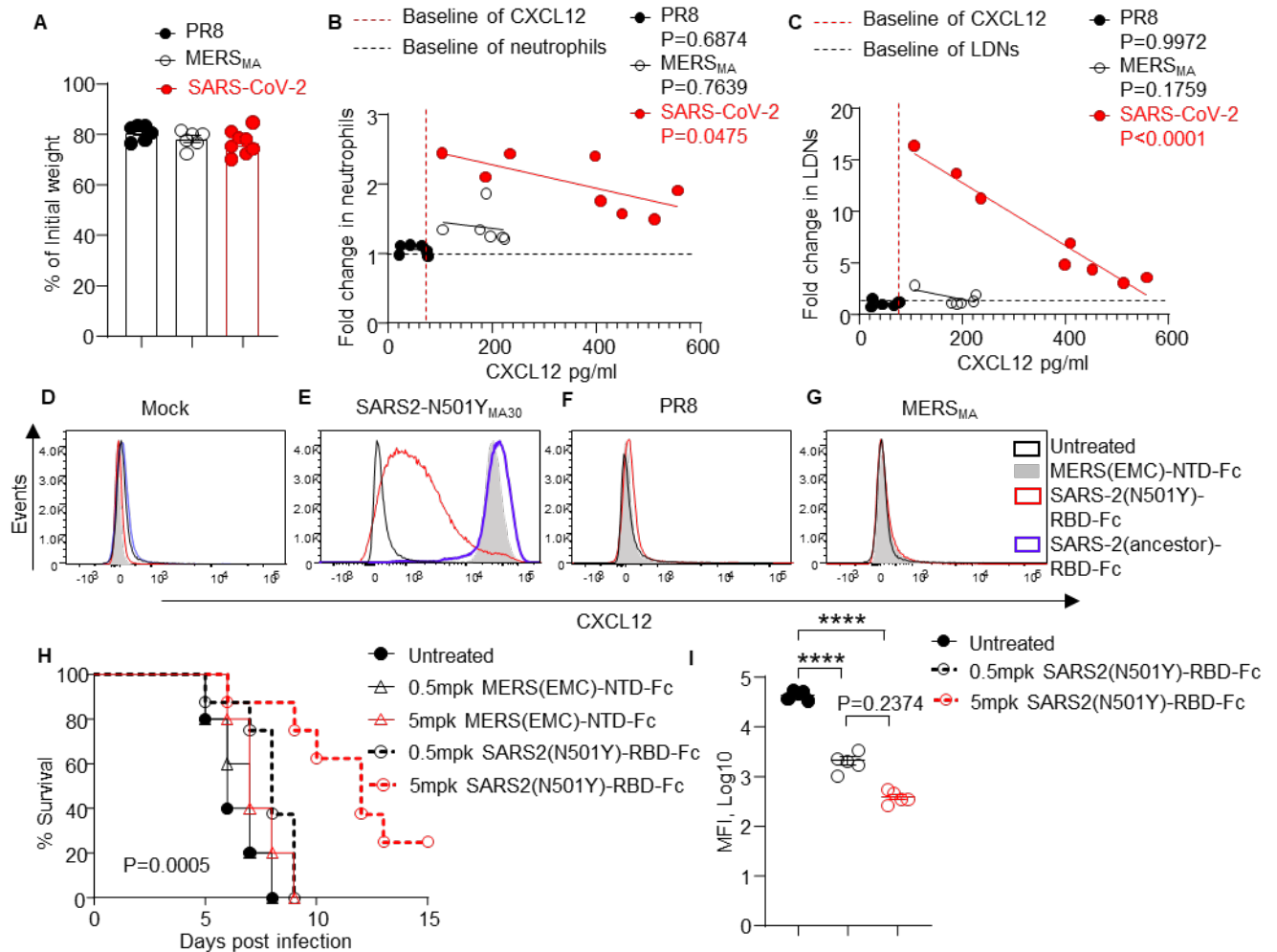es harvested at 5 dpi). Data in (**D**) are mean±SEM (n=8) and are a summary of two independent experiments. LOD, limit of detection. (**E-G**) Numbers of total neutrophils/LDNs (**F**) and CFSE-stained neutrophils/LDNs (**G**) identified in peripheral blood, lung and bone marrow (BM) after treatment with anti-CXCL12 antibody or isotype control (IC, isotype Ig) (n=5) (**E**). Data are mean±SEM and are representative of two independent

1023   experiments. *P< 0.05, ** P< 0.01, ***P< 0.001 by ANOVA F-test in (**F** and **G**). (**H** and **I**)

1024   Survival (**I**) of 8-10-month-old C57BL/6N mice infected with 1000 pfu SARS2-N501Y$_{MA30}$

1025   followed by treatment with anti-CXCL12 antibody, and anti-Ly6G antibody or its isotype control

1026   (IC, isotype Ig) (**H**). Data in (**I**) are summary of two independent experiments (n=8).

Figure 7: SARS-CoV-2-RBD-Fc modifies CXCL12 expression by vascular endothelial cells and the outcome of SARS-CoV-2 infection. (**A**) Weights of mice infected with 500 pfu IAV-PR8 (n=6), 500 pfu MERS$_{MA}$ (n=6), or 5000 pfu SARS2-N501Y$_{MA30}$ (n=8) measured at 5 dpi. (**B** and **C**) Correlation between plasma CXCL12 concentration and fold change of peripheral blood neutrophils (**B**) and LDNs (**C**) in IAV-PR8-, MERS$_{MA}$-, and SARS2-N501Y$_{MA30}$- infected mice at day 5 post infection. (**B**) R-values=0.04474 (P=0.6874) (IAV-PR8), 0.02521 (P=0.7639) (MERS$_{MA}$) and 0.5072 (P=0.0475) SARS2-N501Y$_{MA30}$. (**C**) R-values=3.492e-006 (P=0.9972) (IAV-PR8), 0.4028 (P=0.1759) (MERS$_{MA}$), and 0.9547 (P<0.0001) (SARS2-N501Y$_{MA30}$). Data are representative of two independent experiments. Mock- (**D**) or SARS2-N501Y$_{MA30}$ (5000 pfu)- (**E**), or IAV-PR8 (500 pfu)- (**F**) infected middle-aged C57BL/6N mice (8-10-month-old, n=5/group), or MERS$_{MA}$(500 pfu)-infected *hDPP4*-KI mice (**G**) were treated with 0.5mg/kg weight of MERS (EMC)-NTD-Fc, SARS-2 (N501Y)-RBD-Fc or SARS-2 (ancestral)-RBD-Fc in

1040   0.5ml PBS by i.v. injection at 2 and 4 dpi. Mice were euthanized at 5 dpi and abdominal aorta were

1041   harvested. The expression of CXCL12 in endothelial cells was determined by intracellular staining

1042   via flow cytometry. Data are representative of two independent experiments. (**H** and **I**) 5000 pfu

1043   SARS2-N501Y$_{MA30}$-infected mice were treated with SARS2(N501Y)-RBD-Fc (n=8) or control

1044   (MERS(EMC)-NTD-Fc) (n=5). Survival (**H**) and endothelial cell expression of CXCL12 (**I**) were

1045   determined. ****P<0.01 by ANOVA. Data are mean±SEM and are representative of two

1046   independent experiments. mpk, mg/kg weight.

1047 **Table 1. Patient information of lung sample donors[1].**

Serial NO.	Age	Sex	Days on Ventilator
1	37	M	1
2	69	M	2
3	85	F	0 (DNI)
4	39	F	3
5	48	M	1

1048

1049 DNI: Do Not Intubate.

1050 [1]Only limited patient information is available.

1051 **Table 2. Patient information of PBMC donors.**

General information	
Gender	18 Female (45%)
	22 Male (55%)
Age (years)	Avg. 61.8 (22-95)
	24 White (60%)
	15 Black (37.5%)
Race	1 Native Hawaiian (2.5%)
Date of blood draw	4/21/2020-9/18/2024

1052

Table 3. Convalescent COVID-19 patient data.

General information	Gender	4 Female (44.4%) 5 Male (55.6%)
	Age (years)	Avg. 60 (43-78)
	BMI	Avg. 36.4 (25-56.3)
	History of smoking	4 (44.4%)
Co-morbidities	Cardiovascular disease	8 (88.9%)
	Respiratory system disease	6 (66.7%)
	Renal disease	1 (11.1%)
	Gastrointestinal disease	4 (44.4%)
	Hepatic disease	0
	Hematological disease	0
	Malignant tumor	3 (33.3%)
	Endocrine system disease	7 (77.8%, 6 diabetes mellitus)
	Metabolic disease	5 (55.6%, 5 hyperlipidemia)
	Autoimmune disease	1 (11.1%)
Clinical history	Date of diagnosis	4/29/2020-5/27/2021
	Hospitalization days	21 (7-45) days
	Clinical score (min. P/F[1])	147.6 (92-250)
	ICU care	5 (55.6%)
	Therapy	6 (66.7%) (dexamethasone)
	Reinfection	0
	PACS[2]	5 (55.6%)
	Date of blood draw	4/6/2021-8/20/2021
	Interval between diagnosis and blood draw	206 (43-393) days
Hematology	WBC count	7.77 (3.3-21.8) $\times 10^9$/L
	% lymphocytes	15.05 (0.2-32.2)
	% neutrophils	76.25 (55.1-94.8)

[1]Min P/F: the lowest PaO2 (arterial blood oxygen tension) /FiO2 (Fractional Inspired Oxygen Concentration). P/F 200-300 is indicative of mild ARDS, 100-200 moderate, <100 severe.

[2]Post Acute Sequelae of COVID-19

1058 **Table 4. Most Significant Gene Ontology Biological Processes for Differentially Expressed**
1059 **Proteins.**

Normal Density Neutrophils (NDNs)	Low Density Neutrophils (LDNs)
Neutrophil degranulation	Blood coagulation, fibrin clot formation
Myeloid leukocyte activation	Blood coagulation, intrinsic pathway
Leukocyte mediated immunity	Negative regulation of fibrinolysis
Leukocyte activation involved in immune response	Negative regulation of macrophage cytokine production
Regulated exocytosis	Triglyceride transport
Exocytosis	Nucleosome positioning
Vesicle-mediated transport	Plasminogen activation
Immune effector process	Fibrinolysis
Leukocyte activation	Complement activation, alternative pathway
Secretion by cell	Positive regulation of blood coagulation

1060